2009

Density Functional Investigations of Pure and Ligated Clusters

Kristen Casalenuovo
Virginia Commonwealth University

College of Humanities and Sciences
Virginia Commonwealth University

This is to certify that the thesis prepared by Kristen A. Casalenuovo entitled DENSITY FUNCTIONAL INVESTIGATIONS OF PURE AND LIGATED CLUSTERS has been approved by his or her committee as satisfactory completion of the thesis requirement for the degree of Master of Science in Physics and Applied Physics.

Dr. Shiv N. Khanna, College of Humanities and Sciences

Dr. Dusan Bratko, College of Humanities and Sciences

Dr. Alison A. Baski, College of Humanities and Sciences

Dr. Alison A. Baski, Chair of Physics

Dr. Fred Hawkridge, Interim Dean of the College of Humanities and Sciences

Dr. F. Douglas Boudinot, Dean of the School of Graduate Studies

May 4, 2009

Density Functional Investigations of Pure and Ligated Clusters

A thesis submitted in partial fulfillment of the requirements for the degree of Master of Science in Physics/Applied Physics at Virginia Commonwealth University.

By

Kristen A. Casalenuovo

B.S. in Physics
Longwood University, 2006

M.S. in Physics/Applied Physics
Virginia Commonwealth University, 2009

Director: Dr. Shiv N. Khanna
Professor, Department of Physics

Virginia Commonwealth University
Richmond, Virginia 23284

May 4, 2009

Acknowledgement

This work has been possible only because I stand on the shoulders of giants. First and foremost, I would like to thank my academic advisors along the way. Thank you Dr. Charles Ross for your continued support from Longwood to this day, and for your glowing "walks on water" letters of reference. Thank you Dr. Shiv Khanna, for your wisdom and guidance for my Master's research and education. Your enthusiasm for clusters has been a beacon and a benchmark throughout this process. I would also like to thank my internship advisor for the third study presented in this thesis, Dr. Dirk König at the University of New South Wales. Thank you for being such an affable mentor and for taking a chance on an unknown Master's student from backwoods Virginia. I am eternally enlightened by the mentorship from these advisors, as well as from my group members at VCU. Of the latter, I am especially thankful to Dr. Ulises Reveles for being so optimistic and approachable. Dr. Reveles will stop whatever important project he's working on to help anyone who asks it of him, and do it with a smile on his face. That sort of willingness is rare and he deserves everything he hopes to achieve and more.

Outside of the academic environment, there are some very special people whose encouragement I could not succeed without. I would like to thank my mother Carole, my father Wayne, my brother Andrew, my sisters Donna and Ashley, my best friends Crystal and Janet, and my boyfriend Brett. You all are giants in another sense, equally important; your constant support gives me the courage to reach for my dreams. Thank you all.

Table of Contents

Page

List of Figures and Tables

Page

Abstract

DENSITY FUNCTIONAL INVESTIGATIONS

OF PURE AND LIGATED CLUSTERS

By Kristen A. Casalenuovo, M.S.

A thesis submitted in partial fulfillment of the requirements for the degree of Master of Science at Virginia Commonwealth University, 2009.

Major Director: Dr. Shiv N. Khanna, Professor, Department of Physics

Atomic clusters are attractive candidates for building motifs for new nano-assembled materials with desirable properties. At this nano-regime of matter, the size, shape, and composition of clusters changes their electronic structure and hence their properties. Computational modeling must work hand in hand with experiment to provide robust descriptions of the geometries and energetics of atomic clusters and how they might behave in a nano-assembled material. To this end, we have investigated three distinct species as model systems: antimony oxides Sb_xO_y (x = 1, 2; y = 0 - 3), metal ion-solvent complexes $M_m(NH_3)_n$ (M = Bi, Pb; m = 1 - 2, n = 0 - 4), and quantum dots $Z_{10}H_{16}$ (Z = Si, Ge) and β-$Sn_{12}H_{24}$. Their geometries and electronic structures have been determined using gradient-corrected density functional theory. The relative stabilities for antimony oxides have been examined by the respective comparison of highest-occupied and lowest-unoccupied molecular orbital (HOMO-LUMO) gaps and atomization energies. The superior electronic stability of Sb_2O_3 is indicated by its closed shell

structure, wide HOMO-LUMO gap calculated to be 3.11 eV, and high atomization energy of 4.21 eV. Spin-orbit corrections were necessary for accurate calculation of the metal-solvent energetics, closing the gap between experimental and theoretical values by 1.05 eV for the electron affinity of the Pb atom. Quantum dot modeling of the well-established Si and Ge as well as the less-investigated Sn illuminated the accuracy of the CEP basis sets and the B3LYP functional over other DFT computational routes for clusters containing elements beyond the third row. Throughout, the results correlate well with experiment and higher order *ab initio* methods where data is available. These comparisons validate the accuracy of the computational routes used. This document was prepared in the Linux Ubuntu Open Office Suite 2.4.1.

Chapter 1 Introduction

1.0 Basic Principles

The ability to generate and characterize stable clusters grew from the collaborations between atomic spectroscopists and quantum theorists. The first clusters were detected with mass spectrometers in molecular beam apparati from a supersonic jet source in 1961 independently by Bentley and Henkes. The advent of lasers would further facilitate research in the growing field of cluster science. Breakthroughs in the processing speed of computers enabled computational modeling to flourish as an integral part of cluster research. For the past two years, my Master's research has taught me the necessity of theorists and experimentalists working hand in hand to ensure scientific progress. This relationship is so integral to research that it deserves the distinction of a "zeroth" section in the introduction, much like the zeroth law of thermodynamics. With respect to my particular field of nanoscience, this relationship has produced the following principles:

1. Properties of clusters, like atoms, are rooted in their electronic structures.
2. Electronic structure, and hence properties, change with cluster size, shape, and composition.

3. Computational modeling reveals electronic and geometric structures and can help identify the factors that influence stability, reactivity, and mechanisms of formation.

The rest of this thesis will begin and end with these three principles. Hopefully in between, I will have demonstrated to you their absolute truth.

1.1 Overview

Technological progress hinges on the need for devices and materials with specific functions: solar cells which convert light to electrical energy efficiently, fuels which burn slowly and smoothly. Humanity is quickly approaching the limit on fulfilling these technology needs using naturally-occurring materials. A most pressing example, solar cells based on monocrystalline silicon wafers have a theoretical Shockley-Queisser limit of only 31% conversion efficiency [1]. Because of this limit and the increasing cost of silicon, solar energy will never be commercially competitive with fossil fuels using this material. Second generation thin-film, exotic material technologies drive down the production cost by spreading a thin amount over a glass substrate. However, this method also lowers the maximum possible efficiency considerably; the National Renewable Energy Lab (NREL) holds the record for 20% conversion efficiency for Cu(In,Ga)Se2 thin-film cells while the University of New South Wales (UNSW) has achieved the record for monocrystalline silicon wafers at 25% efficiency. However, the Carnot limit for solar conversion efficiency is 95%. How might progress strive for this goal? Enter nanoscience.

Nanoscience is the design and construction of materials from synthetic, nanometer-sized particles. These so-called nanoparticles and atomic clusters possess properties that are size (i.e., number of atoms), shape (i.e., how those atoms are arranged), and composition (i.e., which elements) dependent. Thus, materials can be constructed with made-to-order properties by judicious choice of nanoparticle building blocks. Atomic clusters containing two to a few hundred atoms constitute a new phase of ultra nanoscale where the properties are determined by the quantum confinement leading to behaviors different from those of individual atoms or bulk solids.

Returning to our example: For solar energy to be competitive with fossil fuels, efficiency needs to be maximized while using low-cost, nontoxic materials. Fitting these criteria, quantum dots are attractive candidates for third generation solar cell devices. Quantum confinement makes optical and transport properties size and spacing dependent, thus a material comprised of quantum dots on a substrate lattice would have a band structure tunable to the needs of the device. Novel quantum dot solar cells have the potential to achieve a conversion efficiency of 66% [2].

Environmentally-friendly energy sources are not the only technologies which stand to benefit tremendously from nano-assembled materials. The field of medicine has enjoyed considerable improvement in targeted drug delivery and tumor detection with gold nanoparticles [3] and metallofullerenes [4], respectively. Electronic memory storage is becoming smaller and more dense with materials designed for their intrinsic magnetic moment or spin properties, so-called spintronics. Stain-resistant clothing, anti-reflective

eye glasses, long-lasting sunscreen, anti-microbial food packaging, all these consumer products achieved their desired properties with nano-assembled materials. The perpetuation of cluster research and the characterization of ever more properties ensures even greater accomplishments to come.

The rest of this chapter will acquaint you with the practical information required for understanding the remainder of this thesis. The next section, §1.2, will be devoted to an introduction of how we determine the properties of clusters with geometries and total energies obtained from density functional theory (DFT). We compare certain calculated properties such as the adiabatic electron affinity (AEA) and vertical detachment energy (VDE) to the results of photoelectron spectroscopy (PES) experiments to validate our computational method. Therefore, in §1.3, I will provide an overview of the fundamental principles of PES, as well as a description of the experimental procedure of our collaborators in the Castleman Group of The Pennsylvania State University. They produced the PES spectra and velocity map images (angle-resolved PES) which I will be presenting to prove the validity of my method and to visually enhance the description of my theoretical results. In Ch. 2, I will begin with a general introduction to *ab initio* methods and the advantages of DFT over others. Next I will explain the underlying principles of DFT, as well as the functionals, basis sets, and software packages that set different DFT methods apart.

Three studies on atomic clusters comprise the essence of this thesis. The first study presented focuses on the selected antimony oxide clusters Sb_2, SbO, SbO_2, and

Sb_2O_3. The relevance of each chosen size will be explained. The geometries and energetics of each will be compared to higher level *ab initio* theory or PES experiment or both. Relative stabilities will be discussed using atomization energies, closed- versus open-shell structure, and HL-gaps as markers. The second study pertains to metal ion-solvent energetics of Bi_m and Pb_m solvated in $(NH_3)_n$ where n = 0 - 4 and 0 - 3 for m = 1 and 2, respectively. The commercial appeal of the metals and solvent chosen will be illuminated. Calculated properties such as AEA and VDE will be discussed and compared to PES spectra, velocity map imaging, and what is expected from solvation. Bonding mechanisms will be explained through the DFT-optimized geometries.

Finally, I will present a quantum dot study I conducted for a summer internship at the University of New South Wales in Sydney, Australia. This is perhaps the most DFT-intensive study undertaken; it involved testing different combinations of functional and basis set to find the optimum routes for the geometry optimization and the subsequent single point energy calculation. There, I have performed about 40 different DFT routes for each approximant: H- and OH- terminated Si_{10}, Ge_{10}, and Sn_{12}. The average bond lengths from each route will be compared to a high-level reference route and the experimental value. Density of states will be presented for each H-terminated approximant as obtained by the high-level reference route and the determined most accurate and efficient method.

1.2 Calculating Properties of Clusters

Properties of atoms are rooted in their electronic structure, specifically in the outermost valence shell. Atoms desire the most stable configuration which is a "closed" shell structure. They tend towards this by donating or accepting electrons, whichever is the fastest route to completely fill the valence shell. The lower their ionization potential, the more willingly they will donate electrons when in the presence of other atoms. The higher their electron affinity, the more willingly they will accept.

The density functional formalism has been the vehicle of this exploration. Computational modeling with a high degree of accuracy determines the properties of atomic clusters and nanoparticle candidates. Modeling complements experiment by revealing otherwise unobservable, fundamental information such as the cluster's physical geometry and total energy for a specified charge state and spin multiplicity.

Properties which can be observed are compared to experiment to validate the computational method. Two such observable properties are the electron binding energy eBE for a particular orbital and the electron affinity EA for a particular cluster species. The adiabatic electron affinity AEA is calculated as the difference in energy between the ground state neutral and the ground state anion:

$$AEA = E_{GSA} - E_{GSN} \quad .$$

A similar property is the ionization potential IP, the difference in energy between the ground state neutral and the ground state cation:

$$IP = E_{GSN} - E_{GSC} \quad .$$

The electron binding energy eBE is the energy required to remove an electron from its atomic or molecular orbital. Here it is calculated from the ground state anion with spin multiplicity M. Also called vertical detachment energy VDE within cluster theory, one is calculated for each possible spin multiplicity the transition to a neutral state could result in (M ± 1):

$$VDE(M \pm 1) = E_{GSA}(M) - E_N(M \pm 1) \quad .$$

To calculate the VDE for the outermost electron in a singly-charged negative ion, a single point energy calculation is taken with the ground state anion's geometry frozen and a neutral charge and M plus or minus one specified. If one of the VDE's calculated values correlates with an eBE peak in the photoelectron spectrum of that particular cluster, it is reasonable to conclude that we have predicted the correct multiplicities for both the anion and neutral states involved. When two or more transitions are correctly predicted, we may further conclude that the anion's initial state is the same for each transition and that theory has assigned the requisite state multiplicities correctly.

Two other useful properties which can be calculated with the total energy output of density functional theory are the atomization energy and the incremental binding energy. A bound system has a lower potential energy than the sum energy of the individual parts; this is what holds molecules and clusters together. The atomization energy per atom E_{atom} is the energy required to break apart a gaseous cluster into its atomic constituents. In general, if you have x number of element A atoms and y number

of element B atoms in an atomic cluster C = xAyB, the dissociation reaction would look like

$$xAyB \rightarrow xA + yB$$

Then E_{atom} is given by

$$E_{atom} = \frac{xE_A + yE_B - E_C}{x + y}$$

If one would like to know the energy required to remove just one atom or ligand molecule L from a cluster C = xAzL, such as in the reaction

$$xAzL \rightarrow xA(z-1)L + L \quad ,$$

one calculates the incremental binding energy IBE:

$$IBE = E_L + E_{C-L} - E_C \quad .$$

The eigenvalues for single particle wavefunctions from a density functional calculation can be interpreted as orbital energies to generate a complete density of states map. Further, the eigenvalues for the highest occupied and lowest unoccupied molecular orbitals HOMO and LUMO, respectively, can be used to approximate the true energy band gap of the cluster. Since this approximation is up to the individual theorist's interpretation of the meaning of the eigenvalues, it is called the HOMO-LUMO gap or the HL gap:

$$HL\,gap = E_{LUMO} - E_{HOMO} \quad .$$

1.3 Experimental Procedure

Every faithful scientist must revere the marriage between experiment and theory to ensure progress in the pursuit of knowledge. The present study and similar density functional investigations utilize photoelectron spectroscopy results to validate the chosen computational routes. Once validated, modeling yields more robust descriptions of the geometric and electronic structure of atomic clusters than would be possible with experiment alone. In particular, photoelectron spectroscopy (PES) probes the valence band structure of gas phase clusters with superior sensitivity.

Instrumentation for PES has evolved with the principles of the photoelectric effect, beginning with the first observation of photoemission by Heinrich Hertz in 1887 [5]. The quantum theory which computational modeling attempts to emulate was born from such observations [6]. Inspired by others' experiments with the photoelectric effect, Albert Einstein first evoked the particle concept for photons [7] by surmising (correctly) the linear relationship

$$eKE = h\nu - \phi \quad .$$

That is, the maximum kinetic energy of the photodetached electron, eKE, is equal to the difference between the energy, $h\nu$, of the incident radiation and the work function, φ, the threshold energy a free electron requires to escape the crystal lattice.

For a gas phase analyte, the work function is zero and the electron binding energy eBE is the sought after parameter which can be compared directly to theory:

$$eBE = h\nu - eKE \quad .$$

In photoelectron spectroscopy PES spectra of intensity plotted against electron binding energy eBE, the eBE for a particular transition is the x-axis value at the maximum of the intensity peak. The electron affinity is inferred as the threshold energy required to for the transition from the ground state anion to the ground state neutral to occur. Therefore, it is taken to be the x-intercept of the positive slope of the ground state transition peak when the peak is steep, or more generally where the intensity falls to about 2% of its maximum value. For very broad peaks, the scientist must exercise intellectual rigor in deciding if and how an electron affinity should be inferred.

The computational routes are confirmed by comparing calculations from theory with the measurable quantities from PES. The experimental electron binding energies of the photoelectrons' precursor orbitals are checked against the respective calculated vertical detachment energies. When the analyte is a singly-charged negative atom, the binding energy of the outermost electron is equal to the electron affinity of the neutral species. In molecular cases, the electron affinity is extrapolated from the photoelectron spectrum as the x-axis intercept of the binding energy peak's slope.

Our experimental collaborators, the Castleman Group at the Pennsylvania State University, conduct negative ion PES studies which require incident radiation in the visible range. Because the outermost electron is more weakly bound in an anion than in the corresponding neutral (i.e., electron affinity is lower than ionization potential), low energy radiation sources can and must be utilized. Lower photon energy means lower photoelectron kinetic energy and thus enhanced sensitivity and spectral resolution.

Radiation in the visible range (1.6 – 3.6 eV) induces photoemission of only that outermost electron. Visible radiation is obtained with lasers such as the single line from an argon ion laser, a Ti:Sapphire (1.55 eV), or the second harmonic outputs of Nd:YAG or Nd:YAF (~2.5 eV).

The technique of velocity map imaging (VMI) complements traditional PES with robust descriptions of the photoelectron angular distribution (PAD) in addition to the kinetic energy distribution. A plane-polarized radiation source enables determination of the photoelectrons' detachment angles with respect to the direction of laser polarization. The asymmetry parameter, β, describes the anisotropy of the PAD, or lack thereof. Distributions with respect to the axis of the light polarization can be parallel (β = 2), perpendicular (β = -1), or isotropic (β = 0). Most likely, the PAD will be some combination thereof, corresponding to a β somewhere between those ranges.

Whereas the kinetic energy distribution reveals the energetics of the photodetachment process, PADs are dependent upon the precursor molecular orbital and the outgoing partial wave composition [8]. For detachment from an atomic orbital, the asymmetry parameter β depends upon the angular momentum quantum number, *l*. It is calculated from the PADs by integrating the intensities at particular angles over the range of radii which contains the transition of interest. The resulting angles are fitted to the differential cross section equation:

$$I(\theta) = \left(\frac{\sigma}{4\pi}\right)\left[1 + \beta\left(\frac{3}{2}\cos^2(\theta) - \frac{1}{2}\right)\right]$$

where σ is the total detachment cross section, θ is the angle between the laser polarization and the photoelectron's velocity vector. This formula also holds for molecules when averaging over all possible rotational orientations [9].

The A.W. Castleman Jr. group at The Pennsylvania State University investigates the geometric and electronic stabilities of ionic clusters with radiation in the visible range. Their molecular beam apparatus, shown in Figure 1.1, is comprised of a magnetic bottle photoelectron spectrometer coupled to a time-of-flight mass spectrometer. This set-up enables mass selectivity of cluster ions and hence the stepwise study of the size evolution of electronic properties.

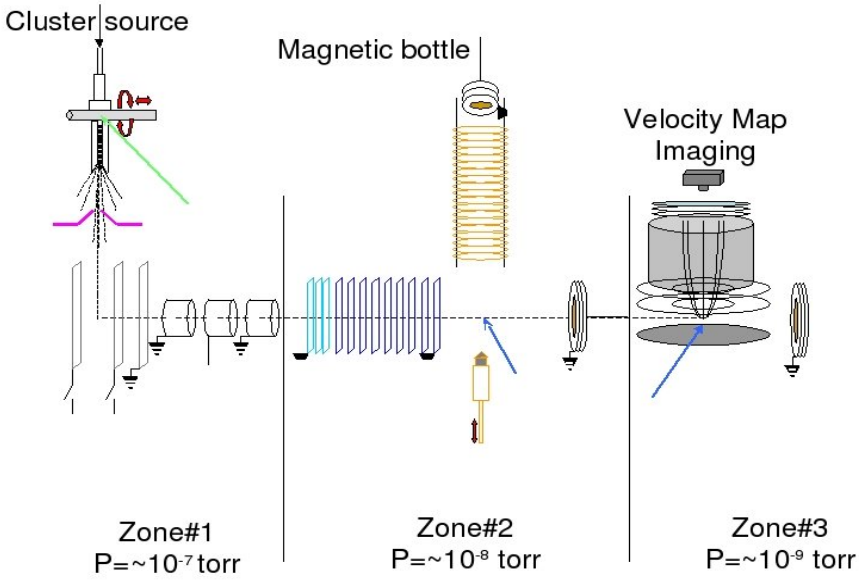

Figure 1.1: Schematic of the molecular beam apparatus, Lola, of the Castleman Group at Penn State [15].

Samples are formed in a laser-induced plasma source with a supersonic jet expansion. The second harmonic output (532 nm) of a neodymium doped yttrium aluminum garnet laser (Nd:YAG) is used [10]. The laser ablates a translating and rotating metal rod to form free radicals and metal ions (Figure A, Zone #1). High purity helium gas (50psi) seeded with 10% solvent (ammonia or oxygen) interacts with the plasma to form various cluster species in a multicollisional environment. The inert carrier gas now mixed with sample clusters undergoes supersonic expansion by escaping the high-pressure reservoir through a conical nozzle pointed downward in the figure. Collisions between the helium and sample clusters transfer vibrational and rotational energies to translational energy. These collisions with the inert gas also cool the translational motion so that the sample clusters have a narrow range of departing speeds when they expand into the vacuum chamber.

After the sample clusters are collimated, they enter a pulsed-grid region (Figure A, Zone #1). The cluster anions are perpendicularly extracted (to the right in the figure) by a high-voltage pulse and accelerated to approximately 1500 eV [10]. Next, they enter a Wiley-McLaren two-stage pulsed electric field time-of-flight mass spectrometer [11] (Figure A, Zone #1). The mass spectrometer measures the relative intensities of the clusters by their mass-to-charge ratio. Mass selectivity with this device ensures the proceeding photoelectron experiment involves only one cluster species at a time. Furthermore, coupling the photoelectron spectrometer to a mass spectrometer enables the

stepwise study of the size evolution of a cluster's electronic properties [12]. The mass spectra may also reveal the relative electronic stability of the most abundant species [13].

The mass-selected ions are focused and decelerated into the detachment region with a series of einzel lenses (Figure A, Zone #2). The detachment laser for the metal-solvent studies, a neodymium doped yttrium aluminum fluoride (Nd:YAF), delivers 527 nm (2.35 eV) radiation from its second harmonic output in nanosecond pulses [14]. In the study of antimony oxides, an excimer laser with 308 nm output is utilized [15]. The photoelectron flight tube is shielded internally and externally from the earth's magnetic field with μ-metal sheets.

Two photoelectron spectrometers, the magnetic bottle analyzer and the velocity map assembly, are respectively utilized for photoelectron detection. The magnetic bottle analyzer (Figure A, Zone #2) collects the photoelectrons in an inhomogeneous magnetic field and detects them simultaneously with a triple z-stack microchannel plate (MCP) [10]. They are analyzed by their kinetic energy, but a PES spectrum of relative intensity versus binding energy is the end result. In the velocity map assembly (Figure A, Zone #3), the photoelectrons are accelerated towards and detected by a position-sensitive 40 mm MCP coupled to a phosphor screen. The MCP is gated to coincide with the arrival time of the photoelectrons [14]. A half-wave plate sets the laser polarization direction to be parallel to the detector surface. The final velocity map images are the accumulation of 20,000 to 40,000 experimental cycles and the intensities are collected using a charge coupled device camera [14].

Chapter 2. Theoretical Method

2.1 *Ab initio* Methods

Ab initio methods grew out of the need for an alternative approach to calculate the observables of a quantum mechanical system. In quantum mechanics, the wave function Ψ contains all the possible information about a system. Operating on Ψ yields an eigenvalue, the value of the observable which the particular operator represents. The hamiltonian of the time-independent Schrödinger's equation contains three such operators:

$$\hat{H}|\Psi\rangle = \hat{T} + \hat{V} + \hat{U}|\Psi\rangle = E|\Psi\rangle$$

the kinetic energy operator $\hat{T}$, the potential energy operator $\hat{V}$, and the Coulomb or electron-electron interaction energy operator $\hat{U}$. Together, these operators act on the wavefunction to yield the total energy E of the system. In the usual Schrödinger's equation above, the system has $3N - 3$ degrees of freedom and requires $3N$ coordinates to define the location of each nucleus and electron in the system. Obtaining the solution then goes from laborious to impossible with the addition of only a few electrons.

Under the Born-Oppenheimer approximation, one reduces the number of variables by decoupling nuclear and electronic degrees of freedom. All the nuclear

degrees of freedom (vibrational and rotational) are contained in an external potential $v(\mathbf{r})$. This potential enters into the equation as the potential energy experienced by the system's electrons which, strictly speaking, is what it is [16]. Founded on the large disparity between the masses of the behemoth nuclei and the much smaller electrons, this is a valid approximation for quantum mechanical calculations. It is useful not only for the quantum mechanical approach but for the *ab initio* methods as well.

To determine the observable properties of a many-body system, the usual quantum mechanical (QM) approach within the Born-Oppenheimer approximation

$$v(\boldsymbol{r}) \overset{SE}{\Rightarrow} \Psi\left(\boldsymbol{r}_1, \boldsymbol{r}_2, \ldots \boldsymbol{r}_N\right) \overset{\langle \Psi|\ldots|\Psi \rangle}{\Rightarrow} observables$$

proceeds by determining $v(\mathbf{r})$ from the location and range of movement of the nuclei and thus the type of system under study: atom, molecule, or solid [16]. Solving Schrödinger's equation (SE) with this potential yields the system's wavefunction dependent solely on the electronic coordinates. The wavefunction can then be used to take the expectation values of the observables of interest.

The major hang up with the QM approach for the many-body problem is the exact solution of Schrödinger's equation. Even within the Born-Oppenheimer approximation, the complexity of the time-independent Schrodinger's equation for more than one electron

$$\left[\sum_i^N \left(\frac{-\hbar^2 \nabla_i^2}{2m} + v(\boldsymbol{r}_i)\right) + \sum_{i<j} U(\boldsymbol{r}_i, \boldsymbol{r}_j)\right] \Psi(\boldsymbol{r}_1, \boldsymbol{r}_2, \ldots, \boldsymbol{r}_N) = E\, \Psi\left(\boldsymbol{r}_1, \boldsymbol{r}_2, \ldots, \boldsymbol{r}_N\right)$$

necessitates an alternative approach. Specifically, the Coulomb operator $\hat{U}$ (the third term in the above equation) is where the exact solution of SE becomes insurmountable for the many-body problem.

Scientists over the years have developed a mélange of methods to bypass the exact solution of Schrödinger's equation yet sufficiently approximate QM observables. These methods include perturbation theory (such as MP2), configuration interaction (CI), and density functional theory [16]. Considered *ab initio* (Latin, "from first"), they are derived from theoretical principles and do not rely on empirical data. Two techniques lie at the heart of these methods; external perturbation and the variational principle. While perturbation, applying an external disturbance to a molecular system, is most useful for determining chemical and physical properties [17], the variational principle is the foundation for methods which aim to uncover electronic and geometric structure.

Density functional theory and almost all other quantum computational methods are formulated with a variational theorem. The variational principle for the total energy states that if the ground state energy of a hamiltonian is calculated using a density that is not the true ground state density, the resulting energy can never be below the true ground state energy:

$$E_v[n_0] \leq E_v[n'] \quad .$$

The original theorem is rightfully attributed to Eckart [17, 18], although the principle is stated above as it applies to the formulation of DFT.

The accuracies of *ab initio* methods are determined by comparing results with experiment and with other theoretical routes. There is a trade-off between accuracy and processing expense with all computational methods. This is not necessarily a linear proportionality. Methods that require much more computational power do not always deliver a significantly higher amount of accuracy. Just as a hypothesis is only as useful as its testability, calculations can only be validated to the extent of the experimental observability. Barring that option, accuracy can only be analyzed by relative comparison to other theoretical methods. It is here where *ab initio* methods are superior over their semi-empirical cousins; their results can be systematically improved so their level of quality is easily assessed [20].

Out of the three *ab initio* methods mentioned, the most versatile is density functional theory (DFT). In its most widely used form, DFT shifts the many-body problem into single-body iterations with the celebrated Kohn-Sham equations. Even though it may arguably be less accurate, DFT retains the universality of Schrodinger's equation in that it can be applied to many different systems [16]: atomic, molecular, and solid state. Its simplification to single-particle orbitals and application of the Hohenberg-Kohn theorems determine the true ground state density and in principle all other observables. In the absence of strong correlations, the Kohn-Sham eigenvalues are empirically shown to approximate the true energy levels and thus band structures of extended systems [16].

2.2 Density Functional Theory

Density functional theory (DFT) rests on two elegant theorems first proposed by Hohenberg and Kohn (HK) [19]. Their formulation of DFT as an exact theory of many-body systems applies to any system of interacting particles moving in an external potential [20]. The first HK theorem states that the external potential $v(\mathbf{r})$ is determined uniquely, up to a constant factor, by the ground state particle density $n_0(\mathbf{r})$. Since the hamiltonian is fully determined, the many-body wavefunction is also determined as a unique functional of the ground state density:

$$\Psi_0 = \Psi[n_0] \quad .$$

Because all possible information about a system is contained in this wave function, the expectation value of any observable must also be a functional of the ground state density:

$$O_0 = O[n_0] = \langle \Psi[n_0] \mid \hat{O} \mid \Psi[n_0] \rangle$$

The second HK theorem follows that one such observable, the ground state energy, can be defined as a universal functional valid for any $v(\mathbf{r})$:

$$E_v[n_0] = T[n_0] + U[n_0] + V[n_0] = T[n_0] + U[n_0] + \int d^3r\, n_0(\boldsymbol{r})\, v(\boldsymbol{r}) \quad .$$

Then the *exact* ground state energy is just the global minimum of this functional for any particular $v(\mathbf{r})$ according to the variational principle and the $n_0(\mathbf{r})$ that minimizes the energy is the *exact* ground state density [20]. The ground state energies and geometries of different charge states for the same species can be used to obtain the ionization potential, electron affinity, vertical detachment energy, molecular binding energy, and density of

states. Although the first HK theorem guarantees all observables are functionals of $n_0(\mathbf{r})$, many of these are not known explicitly.

The most direct DFT approach in light of the HK theorems would be to minimize the ground state energy with respect to the ground state charge density function $n_0(\mathbf{r})$ through a series of iterations.

$$n_0(\boldsymbol{r}) \Rightarrow E_v[n_0] \Rightarrow vary\ v(\boldsymbol{r}) \Rightarrow E_{v,0}$$

For subsequent geometry optimizations, the nuclear degrees of freedom such as the bond lengths or angles between atoms in a molecule are varied by varying the potential $v(\mathbf{r})$ [16]. From these values of $E_{v,0}$, a potential energy surface can be plotted and the minimizing geometry can be determined. In practice however, minimizing the ground state energy is a daunting numerical task, especially for molecules. Also, the functionals $T[n]$ and $U[n]$ are not known explicitly. These problems can be alleviated through the use of single-particle orbitals.

Kohn and Sham took a cue from Hartree and Fock's single-particle *ansatz* to the many-body SE solution. The Hartree-Fock (HF) or self-consistent field (SCF) method treats electrons as moving in a mean electrostatic field defined by all the electrons in the system. It decomposes the many-body wavefunction as the product of single-particle wavefunctions which act as the variational parameters. These electronic orbitals in turn are expanded in an antisymmetric linear combination of atomic orbitals (LCAO) basis set. Solution of the auxiliary SE

$$\left[\frac{-\hbar^2\nabla^2}{2\mathrm{m}}+v(\boldsymbol{r})+v_H(\boldsymbol{r})\right]\phi_i^{HF}(\boldsymbol{r})-q^2\int d^3r'\frac{\gamma(\boldsymbol{r},\boldsymbol{r}')}{|\boldsymbol{r}-\boldsymbol{r}'|}\phi_i^{HF}(\boldsymbol{r}')=\epsilon_i^{HF}\phi_i^{HF}(\boldsymbol{r}')$$

within the HF model proceeds by initializing the determinant wavefunction γ (**r**, **r'**) which can be written as a Slater determinant of single-particle orbitals. The iterative cycles are carried out until the total energy of the interacting hamiltonian is minimized with respect to the determinant wavefunction.

The HF *ansatz* has some advantages and limitations. By assuming the electrons are uncorrelated except that they must obey the Pauli exclusion principle, the exact exchange energy is reproduced [20]. The exchange energy due to the Pauli principle, the tendency for like-spin electrons to avoid each other, is fully accounted for in the term containing γ (**r**, **r'**). Koopman's theorem proves that the HF eigenvalues approximate the excitation energies with great accuracy [20]. However, the correlation energy, the energy due to the coordinated movements between electrons with unlike spins to minimize the repulsion energy, is completely neglected. This weakness is the greatest limitation of HF, causing it to deviate from the total energy in organic molecules by about 27 eV as just one example [17]. Furthermore, the HF equations can only be solved directly in special cases (i.e. - a spherically symmetric atom, a homogeneous electron gas) [20].

In 1965, one year after the HK theorems were published, Kohn and Sham improved upon the HF method with a density functional approach. Density functional theory is considered a post-Hartree-Fock method in that it includes both exchange and

correlation in the hamiltonian while still taking advantage of single-particle orbitals. Kohn and Sham formulated the exact total energy functional

$$E[n] = T[n] + U[n] + V[n] = T_s[\{\phi_i[n]\}] + U_H[n] + E_{xc}[n] + V[n]$$

with the single-particle kinetic energy as an explicit functional of the single-particle orbitals of a noninteracting system

$$T_s[\{\phi_i[n]\}] = -\frac{\hbar^2}{2m}\sum_i^N d^3r\,\phi_i^*(\boldsymbol{r})\nabla^2\phi_i(\boldsymbol{r})$$

and through them, an implicit functional of the density. The Coulomb interaction energy is approximated as the classical electrostatic Hartree energy [16]:

$$U[n] \approx U_H[n] = \frac{q^2}{2}\int d^3r \int d^3r'\,\frac{n(\boldsymbol{r})n(\boldsymbol{r}')}{|\boldsymbol{r}-\boldsymbol{r}'|} \quad .$$

The functional for the exchange-correlation energy $E_{xc}[n]$ is unknown and modern DFT methods mainly differ by their approximation of this term.

The Kohn-Sham (KS) equations treat the ground state electron density $n_0(\mathbf{r})$ as the variational parameter and self-consistently determine it exactly. Kohn and Sham formulated their approach by comparing the minimization condition of the exact total energy functional for a fully interacting system

$$0 = \frac{\delta E[n]}{\delta n(\boldsymbol{r})} = \frac{\delta T_s[n]}{\delta n(\boldsymbol{r})} + \frac{\delta V[n]}{\delta n(\boldsymbol{r})} + \frac{\delta U_H[n]}{\delta n(\boldsymbol{r})} + \frac{\delta E_{xc}[n]}{\delta n(\boldsymbol{r})} = \frac{\delta T_s[n]}{\delta n(\boldsymbol{r})} + \nu(\boldsymbol{r}) + \nu_H(\boldsymbol{r}) + \nu_{xc}(\boldsymbol{r})$$

to its minimization condition for a noninteracting system

$$0 = \frac{\delta E_s[n]}{\delta n(\boldsymbol{r})} = \frac{\delta T_s[n]}{\delta n(\boldsymbol{r})} + \frac{\delta V_s[n]}{\delta n(\boldsymbol{r})} = \frac{\delta T_s[n]}{\delta n(\boldsymbol{r})} + \nu_s(\boldsymbol{r}) \quad .$$

These differential equations show that the solution for both will be the same if the effective potential v_s is chosen to be [16]

$$v_s(\boldsymbol{r}) = v(\boldsymbol{r}) + v_H(\boldsymbol{r}) + v_{xc}(\boldsymbol{r}) \quad .$$

Incorporating all the difficult many-body terms into v_s , the auxiliary noninteracting hamiltonian may act on single-particle (KS) orbitals

$$\left[\frac{-\hbar^2\nabla^2}{2\mathrm{m}} + v_s(\boldsymbol{r})\right]\phi_i^{KS}(\boldsymbol{r}) = \epsilon_i\phi_i^{KS}(\boldsymbol{r}) \quad .$$

Since the exact $n_0(\mathbf{r})$ is equivalent to the $n_0(\mathbf{r})$ of noninteracting particles according to the two minimization conditions (i.e. - "noninteracting *v*-representability"), solving for the KS orbitals reproduces the true electron density of the interacting system

$$n(\boldsymbol{r}) \equiv n_s(\boldsymbol{r}) = \sum_i^N |\phi_i(\boldsymbol{r})|^2$$

once self-consistency is achieved. Therefore, the above three equations are referred to as the KS self-consistent field (SCF) equations. It is possible in DFT to use other equations. For systems where relativistic effects are significant, the formulation of SCF equations from the relativistic Dirac equation may be preferred.

Up until this point, we have ignored spin in our formulation of density functional theory (DFT). For the most general form of DFT, the density must be linearly separated into two variables; one for the spin-up electrons and one for the spin-down

$$n(\boldsymbol{r}) = n^{\uparrow}(\boldsymbol{r}) + n^{\downarrow}(\boldsymbol{r}) \quad .$$

Likewise, the effective potential v_s is separated into two variables conjugate to each spin density. The functionals must also be constructed to take the different spin densities into account. Other than that, spin-DFT calculations proceed from the HK theorem and the KS equations exactly as described above.

The genius of the KS *ansatz* lies in the construction of the kinetic energy T_s as an explicit functional of single-particle orbitals and an implicit functional of the interacting density. By separating out T_s and containing the Coulomb interactions in U_H, the exchange correlation energy $E_{xc}[n]$ can be approximated as a local or semilocal functional of the density [20]:

$$E_{xc}\left[n^{\uparrow}, n^{\downarrow}\right] = \int d^{3} r\, n(\boldsymbol{r})\epsilon_{xc}([n], \boldsymbol{r})$$

where ϵ_{xc} is the energy per electron at point **r** and depends only upon the density $n(\mathbf{r}, \sigma)$ near point **r**. Only the total density appears in the integrand because Coulomb interactions are independent of spin [20]. For spin-polarized systems, the different spin densities are accounted for in ϵ_{xc} .

2.3 Functionals in Practice

The true ground state density $n_0(\mathbf{r})$ determined from the KS equations can be used to calculate any observable according to the HK theorem, as long as the exact density functional is known. The total ground state energy could be calculated directly using the exact energy functional, however the explicit E_{xc} functional is unknown. Instead, approximate functionals are employed to calculate the total energy. Two widely-used

examples are the local density approximation (LDA) and the generalized gradient approximation (GGA).

The LDA, or more generally the local spin density approximation (LSDA), works best for solids, such as nearly-free-electron metals, which are similar to a homogeneous electron gas (the so-called Jellium model). In such cases, the range of the exchange and correlation effects is very short [20], thus the charge density can be assumed to be fairly constant throughout the system. Accordingly, the exchange correlation functional is constructed as an integral over all space with the same exchange correlation energy per electron as a homogeneous gas ϵ_{xc}^{hom} which is a function of the density and spin:

$$E_{xc}^{LSDA}\left[n^{\uparrow}, n^{\downarrow}\right] = \int d^3 r\, n(\boldsymbol{r})\epsilon_{xc}^{hom}(n^{\uparrow}(\boldsymbol{r}), n^{\downarrow}(\boldsymbol{r})) \quad .$$

The limitations and successes of the LSDA are grounded in its assumption of the density as slowly varying. Unlike in the HF method where the cancellation of self-interaction terms is exactly canceled by the non-local exchange interaction, it is only approximate in LSDA. This effect is small in homogeneous systems, but highly nontrivial in confined systems such as atoms [20]. Even for inhomogeneous cases however, the LSDA works well in practice because the exchange-correlation hole is exact for some hamiltonian, just not the correct one. Therefore, the hole obeys constraints imposed by sum rules, a feat which is difficult to accomplish with arbitrary approximations [20].

By incorporating the magnitude of spin density gradients into the functional, the GGA is considered a semilocal approximation:

$$E_{xc}^{GGA}\left[n^{\uparrow}, n^{\downarrow}\right] = \int d^3 r\, n(\boldsymbol{r})\epsilon_{xc}(n^{\uparrow}, n^{\downarrow}, |\nabla n^{\uparrow}|, |\nabla n^{\downarrow}|, \ldots)$$

$$\equiv \int d^3 r\, n(\boldsymbol{r})\epsilon_x^{hom}(n) F_{xc}(n^{\uparrow}, n^{\downarrow}, |\nabla n^{\uparrow}|, |\nabla n^{\downarrow}|, \ldots) .$$

Here $\epsilon_x^{hom}(n)$ is the exchange energy per electron of the unpolarized homogeneous gas. The exchange-correlation enhancement factor F_{xc} is dimensionless and is linearized as the sum of F_x and F_c. With the form of $\epsilon_{xc}^{hom}(n, \sigma)$ being well-established, different GGA's are distinguished only by their treatment of F_x and F_c. Different F_x's agree in value for small density gradients so all GGAs yield similar improvement over LDA by lowering the exchange energy within that range [20]. The exchange energy is lowered more for atoms than for molecules and solids because the former's density gradients vary more rapidly, thus correcting LDA's overestimation of binding energies. All GGA's recover the E_x in the uniform gas limit by imposing the constraint that $F_x = 1$ in that region.

The GGA provides improved agreement to experiment over LDA by modifying the behavior of the E_{xc} functional at large density gradients to preserve pertinent physical conditions in those regions. Constraints are imposed through the construction of F_x and F_c. For instance, Becke (B88-GGA) chose F_x with empirical coefficients to give the correct exchange energy density ϵ_x. Perdew and Wang's (PW91) GGA satisfies the Lieb-Oxford bound and contains a non-uniform scaling condition (with coefficients derived from Monte Carlo data) to reproduce the correct exchange in the high gradient limit [20]. Alternatively, the numerical parameterization of Perdew, Burke, and Enzerhof (PBE) retains the correct energetic features of PW91 albeit in a more simplified,

accessible form [21]. The PBE-GGA's vanishing correlation term for rapidly varying density makes it highly accurate for strongly delocalized systems. Its purely theoretical approach and superior reliability makes PBE the functional of choice for many electronic structure calculations.

Hybrid functionals are the most accurate in terms of energetics due to their mixing of HF exact exchange, a nonlocal quantity, and DFT exchange-correlation. The contribution of each to E_{xc} is linear and scaled by respective coefficients. The functional is constructed with the constraint that it recover the uniform electron gas limit. Becke determined the values of the coefficients for B3LYP semiempirically [22] which turn out to work well for many types of molecules.

$$E_{xc}^{B3LYP} = E_{xc}^{LSDA} + a_0(E_x^{HF} - E_x^{LSDA}) + a_x \Delta E_x^{B88} + a_c \Delta E_c^{LYP}$$

Here Δ denotes the respective gradient corrections to the LSDA. Becke's coefficients (a_0=0.20, a_x=0.72, a_c=0.81) work with other hybrid three-parameter functionals as well, but can be changed manually to suit the needs of the system. For instance, the second term replaces some local exchange with the exact exchange, thus a_0 depends on the coupling-dependence of the exact E_{xc} [h].

For those who desire to retain the purely numerical nature of DFT, Perdew, Ernzerhof, and Burke [23] proposed the form

$$E_{xc}^{hyb} = E_{xc}^{LSDA} + \frac{١}{٤}(E_x^{HF} - E_x^{GGA})$$

for their hybrid functional. The coefficient 1/n is chosen from the lowest order n of perturbation theory necessary to describe the shape or coupling dependence of the exact E_{xc}. The accuracy of Moller-Plesset fourth-order perturbation theory for most molecules suggests n=4 as the most general choice. Optimally, one may change n depending on the system and property of interest [23]. The PBEPBE hybrid is similar in performance to B3LYP, without the semiempirical formulation. In practice, hybrid functionals compensate the errors respectively present in lone HF and DFT [17].

2.4 Basis Sets

To solve the HF or KS equations, the *N*-electron wave function is expanded in products of one-electron orbitals. These orbitals in turn are described by primitive basis functions which form the orbital basis set:

$$\phi_i = \sum_{\mu}^{N} c_{i\mu}\phi_\mu \quad .$$

Although these are ultimately approximations of true molecular orbitals (MOs), they can be highly accurate if the proper ones are chosen. In general, basis sets are chosen to describe the aspects of the orbitals and one is specified for each element in the system. Thus, the type of atom (i.e., number of electrons) and level of accuracy and/or efficiency required must be taken into consideration. There are two types of basis sets employed for this study: scalar relativistic pseudo-potentials and all-electrons constructed with a linear combination of atomic(-like) orbitals (LCAO).

Pseudo-potentials replace the Coulomb potential of the nucleus and the rapidly-varying effects of the tightly bound core electrons with a smoothly-varying effective potential. Pseudo-potentials are constructed with a feasible number of plane waves. Relativistic and spin-orbit effects can be built into the pseudo-potential by deriving them from a fully relativistic hamiltonian. Because core electrons are highly localized, scalar relativistic pseudo-potential basis sets retain a high degree of accuracy and are more efficient for larger clusters and clusters containing heavy atoms. They are the optimal choice for describing the band structure in solids in the nearly-free electron approximation (i.e., sp-bonded metals and semiconductors) [20].

All-electron LCAO basis sets contain functions which represent localized atomic or atomic-like orbitals. Sometimes referred to as primitive basis functions, these atom-centered orbitals need only be specified by the symmetry of the angular momentum, *l,* as products of radial functions and spherical harmonics [20]. Since they consider all the electrons of the cluster, they may not computationally feasible for larger atoms. However, LCAOs are highly accurate for small clusters of atoms up to the third row.

The two flavors of atomic-like orbitals used to construct LCAO basis sets are Gaussian-type (GTO) and Slater-type (STO) orbitals. GTOs are easier to work with numerically, since the product of any two gaussians is another gaussian. Thus, all multi-center integrals can be evaluated with them analytically, unlike with the original STOs [20]. STOs have the advantage of more closely resembling atomic orbitals; GTOs are eigenstates of a harmonic oscillator. STOs have been revamped by expanding them in

terms of GTOs so that they are easier to handle numerically while still offering a more realistic potential. With STOs, the coefficients in front of the gaussians are fixed so they can be used to compare calculations with identical bases or achieve systematic accuracy with different bases [20].

Extended basis functions further increase accuracy for LCAOs by accounting for the differences in the shapes of the orbitals. Two or more radial functions instead of one for the same l accommodate a larger range for decaying wavefunctions. The nomenclature for basis sets is tied to the number of radial functions used: single-zeta or "SZ", double-zeta or "DZ", and triple zeta or "TZ." Split valence basis sets (denoted by "V") allow one to do this more efficiently by calculating multiple radial functions for the valence orbitals only since the shapes of the core orbitals differ trivially. Polarization functions ("P" or "*") can be added to handle the nonspherical charge distributions of atoms in molecules or solids. These effectively add a function one l higher than the maximum occupied state in the atom. Finally, a description of anions or weak bonds can be more accurately considered by adding diffuse functions (denoted "+" or "aug").

2.5 DFT Software Packages

Software packages have been developed to systematically carry out electronic structure calculations. Many packages offer not only DFT solutions, but also other *ab initio* methods such as MP2 and CI. The three codes used for this study are Gaussian 03 [24], deMon2k (density of Montreal) [25], and ADF (Amsterdam Density Functional) [26] . In general, users specify the exchange-correlation functional, the basis set, and the

initial geometry. They may also set the self-consistent field convergence criteria and choose to perform a geometry optimization or just a single-point energy calculation. The codes are adapted to perform calculations within certain basis sets. In particular, Gaussian 03 and deMon2k employ GTOs in their bases while ADF uses STOs.

The deMon2k package circumvents solving the four-center repulsion integral with an auxiliary basis set called Gen-A2 (default) or Gen-A2* (with polarization functions). This auxiliary basis essentially turns the four-center integral, which scales by N^4, into a less-expensive three-center integral and introduces a variational fitting of the Coulomb potential. Other programs have similar variational treatments of the Coulomb integral in order to decrease the computational expense of iteratively solving the Kohn-Sham total energy functional; ADF calls theirs charge fitting sets.

The antimony oxide study was carried out with the deMon2k code. The exchange and correlation energy corrections were approximated with the gradient-corrected functional of Perdew, Berke, and Ernzerhof (PBE96) [21]. Due to their relatively small size, the basis set was chosen to be an all-electron LCAO with double zeta split valence polarization (DZVP-GGA), optimized for use in conjunction with GGAs.

The basis sets employed for bismuth and lead solvated in ammonia varied by software. For both the deMon2k and subsequent ADF runs, the functional chosen for the exchange-correlation potential was the PBE GGA. The initial calculations carried out in deMon2k used Dunning's augmented correlation-consistent basis sets, Aug-cc-pVnZ (n = number of radial nodes, here 2 or D). These are designed to converge to the complete

basis set limit. To increase efficiency, these LCAO bases were mixed with relativistic effective core potentials (RECPs) for 23 and 22 frozen core electrons for bismuth and lead, respectively. The basis sets for nitrogen and hydrogen remained pure all-electron DZVP-GGA, meaning the LCAO was optimized for use with a generalized gradient-corrected (GGA) functional.

The geometry optimizations were carried out in internal redundant coordinates using a quasi-Newton method with a Levenberg-Marquardt step restriction. This is the default and most efficient method for deMon2k. ADF has a similar option to utilize delocalized coordinates rather than perform the more computationally expensive Cartesian geometry optimization. The geometries that yield the lowest energy within each charge state are taken to be the respective ground state configurations. The optimized geometries from deMon2k for the solvation study were subsequently fed into ADF.

The DFT program ADF can calculate relativistic spin-orbit effects for a better approximation of the energetics. By construction, using Kohn-Sham SCF equations, deMon2k can not produce spin-orbit corrections. ADF on the other hand offers the Dirac formalism, so that all relativistic effects including spin-orbit are accounted for. The geometries were re-optimized to validate the molecular structures, and as expected did not vary drastically from those optimized in deMon2k. The basis sets used in ADF were TZP's with scalar relativistic pseudo-potentials applied to frozen cores up to and including the 5*p* shell (54 electrons) for both bismuth and lead. Nitrogen and hydrogen were again described solely by the TZP so as to consider all electrons.

To calculate the spin-orbit correction to the energy, the spin can no longer be defined in terms of up and down or alpha and beta. Therefore, spin multiplicities can not be specified. Instead, the collinear approximation was used where the spin at each point in space is associated with the same direction. ADF sets up the basis for spin-orbit calculations in symmetrized fragment orbitals (SFO) for the valence and are orthogonalized with the core orbitals. These orbitals are the irreducible representations of the molecular symmetry group in the spin-collinear approximation. We produced spin-orbit corrected DFT energetics in a single-point energy calculation with the geometries optimized in a previous run without the SFO basis.

Quantum dot calculations were carried out using the Gaussian 03 software package [24]. This study is unique from the others in that it tested different combinations of basis set and functional to determine the optimum computational route for accuracy with affordable expense. The computations were handled by a 440 GFLOPS Linux cluster with 72 cores (64 bit) using a maximum of four parallel processors for each single data run. The functionals utilized were HF (Hartree Fock exact exchange) and hybrid functionals B3LYP (Becke ’88 exchange, Lee-Yang-Parr correlation), B3PW91 (Becke ’88 exchange, Perdew-Wang correlation), and PBEPBE (Perdew-Burke-Ernzerhof ’96 exchange and correlation).

These functionals were paired with the all-electron basis sets: UGBS (relativistic corrections) from de Castro, Jorge, et al; 3-21G*, 6-31G(d), and 6-311+G(2d,p) (split-valence extended sets that do not consider relativistic effects but work well) from the

Pople group; and DGDZVP (DZ and valence polarization from *DGauss* developers). Also tested were scalar-relativistic pseudo-potentials: LanL2MB (minimal basis) and LanL2DZ (extended with DZ) using the Los Alamos effective core potential; and CEP-4G (minimal), CEP-31G, and CEP-121G (both split-valence) from Stevens, Basch, and Krauss.

Chapter 3. Results

3.1 Antimony Oxide Clusters

The unique catalytic, optical, and structural properties of antimony trioxide (Sb_2O_3) are well-known [27] and are commonly exploited in commercial and scientific applications. It has long been used as a flame retardant in plastics, paints, adhesives, and textile backing [28] and as an opacifying agent in optical glass, light bulbs, light emitting diodes, and television tubes. Its large and direct optical band gap in the near-UV region makes Sb_2O_3 thin films an attractive material candidate for optoelectronic devices and solar cell technology [29]. Recent research has elucidated its further potential as an anode material in Li-ion batteries [30, 31]. Nano-scale hierarchical structures of Sb_2O_3 have been fabricated to characterize superhydrophobic properties [32]. Gas-phase antimony oxide clusters are also model systems to investigate how chemical properties change via stepwise cluster formation using experimental techniques such as molecular beam mass spectrometry [33] and photoelectron spectroscopy.

Here we present the first theoretical investigation of selected cluster sizes Sb_xO_y ($x = 1, 2$; $y = 0 - 3$) to illuminate the composition-dependence of properties which makes clusters so attractive for building motifs in nano-assembled materials. We begin with an analysis of Sb_2 to see how antimony behaves if the oxygen is replaced by another Sb.

Next we move on to SbO and SbO_2 to validate the chosen computational route by comparison to photoelectron spectra and by matching structures and electronic transitions to higher level theory. Finally we present the results of Sb_2O_3 and in particular the properties which make this structure so stable.

Theoretical studies of the size evolution of antimony oxide clusters are sparse in the literature. Pure antimony clusters are well-characterized [34-36 and references therein]. Density functional theory (DFT) was used to investigate the crystalline structures of neutral and cationic antimony oxides only [37]. Lee *et al.* conducted in-depth DFT and higher level *ab initio* calculations for the low-lying states of SbO_2 [33]. To date, there have been no studies reporting the stepwise size dependence of geometric and electronic structures of antimony oxides.

The Sb_2 dimer is an excellent cluster to initiate this investigation as there is a plethora of empirical and theoretical data in the literature for comparison. The results obtained here agree very well with other studies, shown explicitly in Table 3.1.1. Zhou et al. [34] also used the PBE functional but with a different basis. Gausa et al. [35] used the slightly older B88 and P86 gradient corrections to the LSDA. Their basis was a TZ-LCAO mixed with a pseudo-potential for a 36 electron frozen core in ADF (so STO primitives). The experiments cited [35, 36] employed negative ion photoelectron spectroscopy coupled to a time-of-flight mass spectrometer, similar to the apparatus of our Penn State collaborators. To determine the bond lengths, they fitted Franck-Condon simulations to their experimentally determined Sb_2 electronic bands.

Sb_2: Methods	R^-	R^0	AEA	VDE(M-1)	VDE(M+1)	E^-_{atom}	E^0_{atom}
PBE/DZVP (This work)	2.65	2.54	1.14	1.22	2.53	1.75	1.64
Other theories	2.65[a]	2.55[a]	0.94[a]	1.39[b]	---	1.85[a]	1.59[a]
Experiment[35] 1	---	2.49	1.25	1.34	2.53	---	1.55
Experiment[36] 2	2.57	2.48	1.28	1.35	2.53	1.66	---

Table 3.1.1: Bond lengths R (Å), adiabatic electron affinity AEA (eV), vertical detachment energies VDE (eV) for transitions from the ground state anion with multiplicity M to the neutrals with multiplicities M-1 and M+1, and atomization energy E_{atom} (eV/atom) for neutral and anionic Sb_2. a- Ref. [34] and b- Ref. [35]

SbO is less investigated than Sb_2. Fortunately our collaborators at Penn State, specifically Ujjwal Gupta, performed photoelectron spectroscopy with a 308 nm excimer laser (4.03 eV detachment energy) to obtain the spectra shown in Figure 3.1.1. The results for this experiment, this investigation, and another theoretical study by Reddy are presented in Table 3.1.2. The comparative theoretical study used a DZ-LCAO basis mixed with an effective core potential (ECP) for Sb with 36 core electrons and for O with two core electrons. Their functional was LSDA with Vosko *et al.* parametrization [37]. Our computational results agree very well with the previously calculated bond length of Reddy and fairly well with the transition energy and electron affinity determined from the photoelectron spectra. The electronic ground state for SbO^- is $^3\Delta$ and for neutral SbO $^2\Pi$.

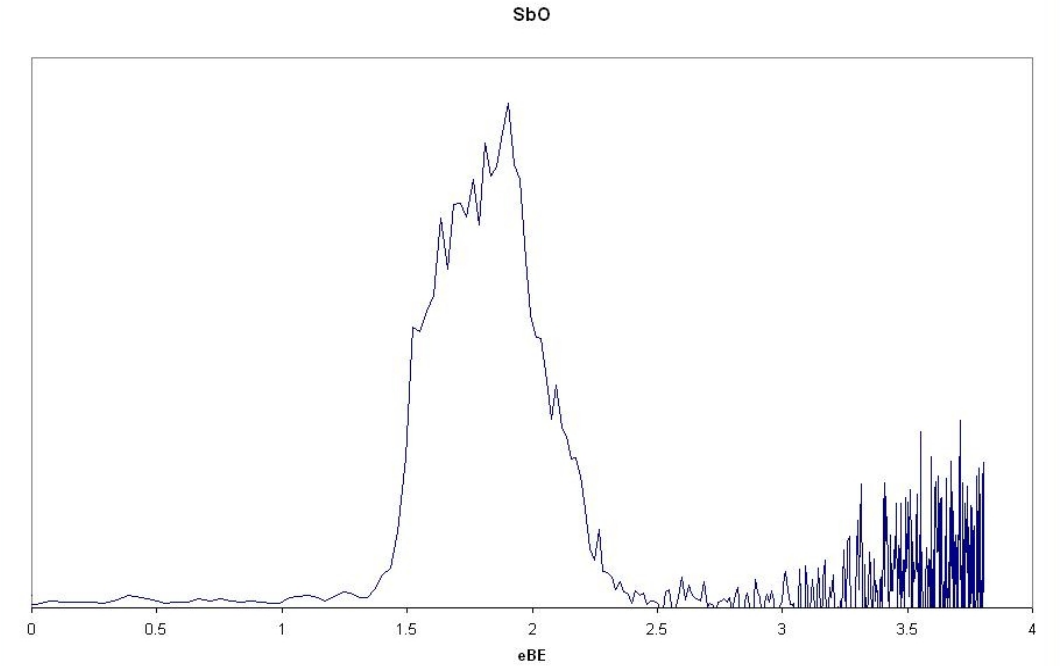

Figure 3.1.1: Photoelectron spectra for SbO. The intensity (y-axis) is in arbitrary units and is plotted against the electron binding energy eBE (eV).

SbO: Methods	R^-	R^0	AEA	VDE(M-1)	VDE(M+1)	E^-_{atom}	E^0_{atom}
PBE/DZVP (This work)	1.94	1.88	1.60	1.66	4.30	2.60	2.25
Experiment (Penn State)	---	---	1.40	1.80	---	---	---
Theory[37]	---	1.84	---	---	---	---	2.70

Table 3.1.2: Bond lengths R (Å), adiabatic electron affinities AEA (eV), vertical detachment energies VDE (eV) for transitions from the ground state anion with multiplicity M to the neutrals with multiplicities M-1 and M+1, and atomization energy E_{atom} (eV/atom) for the neutral and anionic SbO.

Five initial geometries were optimized within each multiplicity/charge state for SbO_2. The geometries for neutral $^2SbO_2$ are depicted in Figure 3.1.2. The ground state, bond angle 123˚, is defined by $^2A_1$ molecular orbital symmetry while the first isomer with the 90˚ bond angle is $^2B_2$**.** The second, linear isomer is a $^2\Sigma_g^+$ state. The geometrical parameters and relative energies are compared to the higher level *ab initio* method, spin-restricted coupled cluster theory RCCSD(T), from Ref. [33]. Those results are summarized in Table 3.1.3. The first isomer's relative energy to the ground state was determined here as 0.16 eV, strikingly close to the higher level calculation of 0.22 eV. The linear isomer's relative energy to the ground state was found to be 0.74 eV, agreeing fairly well with the 0.87 eV predicted by RCCSD(T). The only disparate value was the relative energy for the $^2B_1$ state. Overall, the ordering of the isomers relative to the ground state energy, the bond angles, and the bond lengths calculated with GGA-DFT are consistent with one of the most accurate *ab initio* methods available [17, p.212].

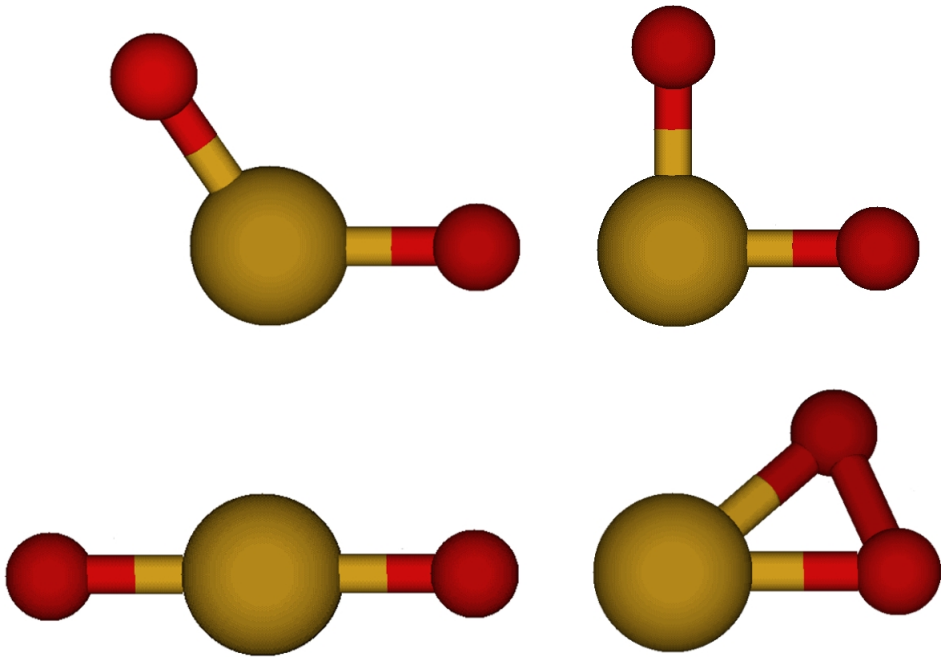

Figure 3.1.2: $^2SbO_2$ neutral geometries of low-lying doublet states. The ground state is in top left corner. The third isomer (bottom right corner) had a relative energy of 2.82 eV thus was not included in further calculations.

SbO_2: Methods	State	E_{rel} (eV)	R	θ
DFT (This work)	$^2A_1$	0.0	1.89	123.56
	$^2B_2$	0.16	1.92	89.60
	$^2\Sigma_g^+$	0.74	1.91	180.0
RCCSD(T)[33]	$^2A_1$	0.0	1.84	122.81
	$^2B_2$	0.22	1.86	89.13
	$^2\Sigma_g^+$	0.87	1.86	180.0

Table 3.1.3: Sb-O bond lengths R (Å) and O-Sb-O bond angles θ (degrees) of neutral $^2SbO_2$ ground state $^2A_1$ and isomers as compared to higher level method.

Anion geometries for SbO_2 were also optimized in order to calculate the vertical detachment energy (VDE) and adiabatic electron affinity (AEA). The $^1SbO_2^-$ structures are shown in Figure 3.1.3. The results for the energetics of the SbO_2 clusters are summarized in Table 3.1.4. The only vertical detachment energy is for m+1 because the anion is a singlet state. The experimental VDE and AEA are obtained from the photoelectron spectra, presented in Figure 3.1.4, obtained by Ujjwal Gupta at Penn State.

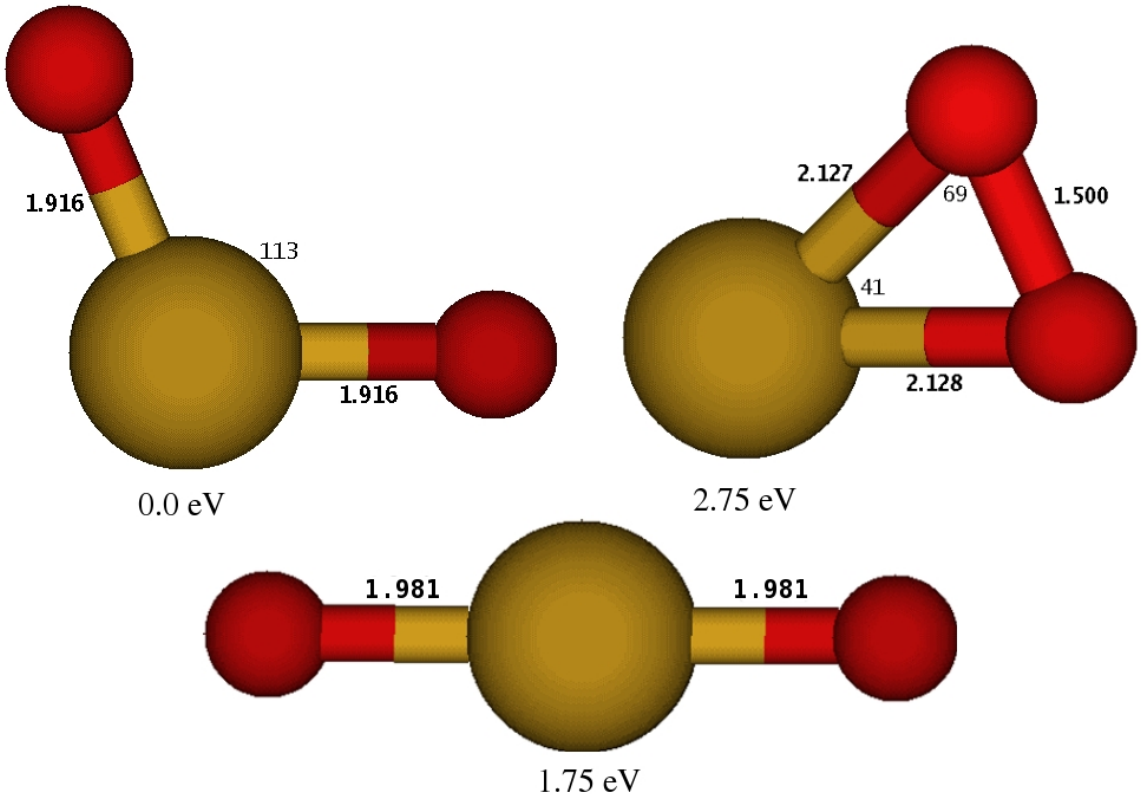

Figure 3.1.3: $^1SbO_2^-$ anion geometries. Underneath each is their energy relative to the ground state. All bond lengths are in units of angstroms (Å).

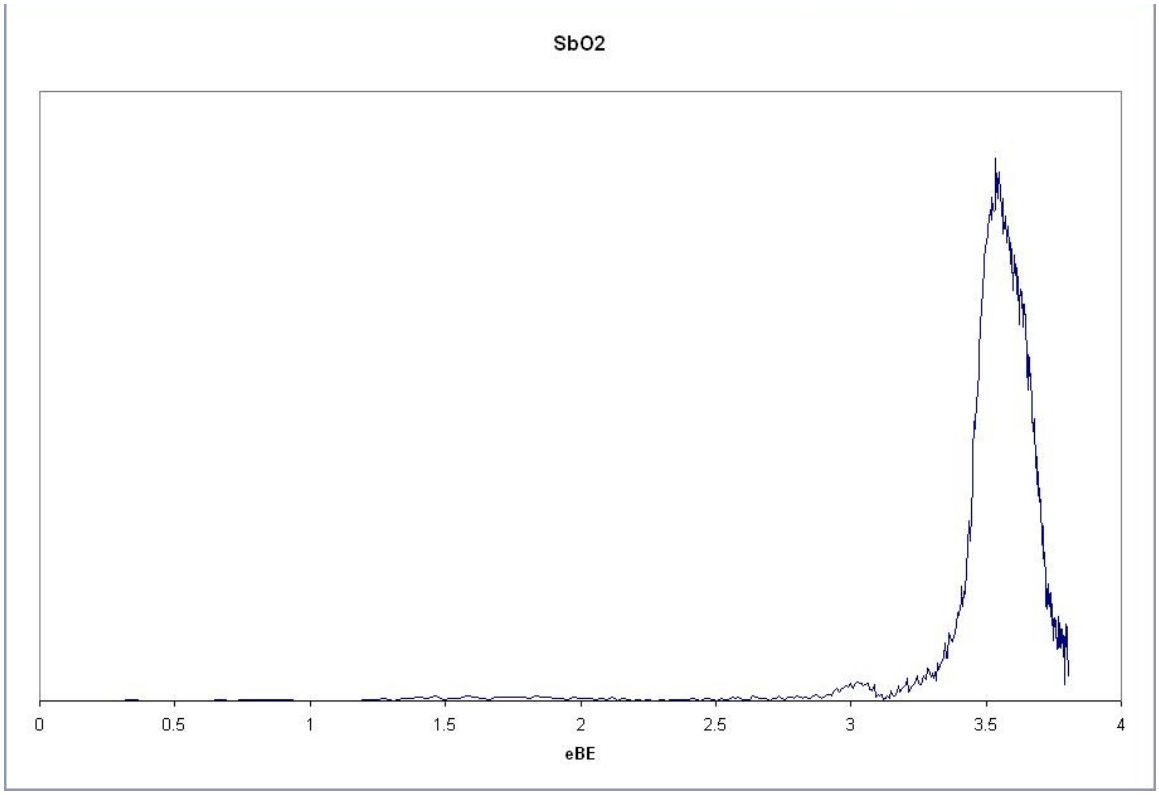

Figure 3.1.4: Photoelectron spectra for SbO_2. The intensity (y-axis) is in arbitrary units and is plotted against the electron binding energy eBE (eV).

SbO_2: Methods	AEA	VDE	E^-_{atom}	E^0_{atom}
GGA-DFT	3.13	3.20	3.53	2.71
Experiment	3.25	3.50	---	---

Table 3.1.4: Adiabatic electron affinity AEA (eV), vertical detachment energy VDE (eV) from the ground state anion singlet (M=1) to the neutral doublet (M=2), and atomization energy (E_{atom} in eV/atom) for the anion and neutral SbO_2.

Seven initial geometries were optimized for each multiplicity (one through six) of the respective anion and neutral Sb_2O_3. The neutral ground state was found to be a singlet state and the ground state anion a doublet state. The low-lying states' geometries and parameters are given in Figure 3.1.5 and Figure 3.1.6 for the neutral and anion, respectively, along with their relative energies to the ground state.

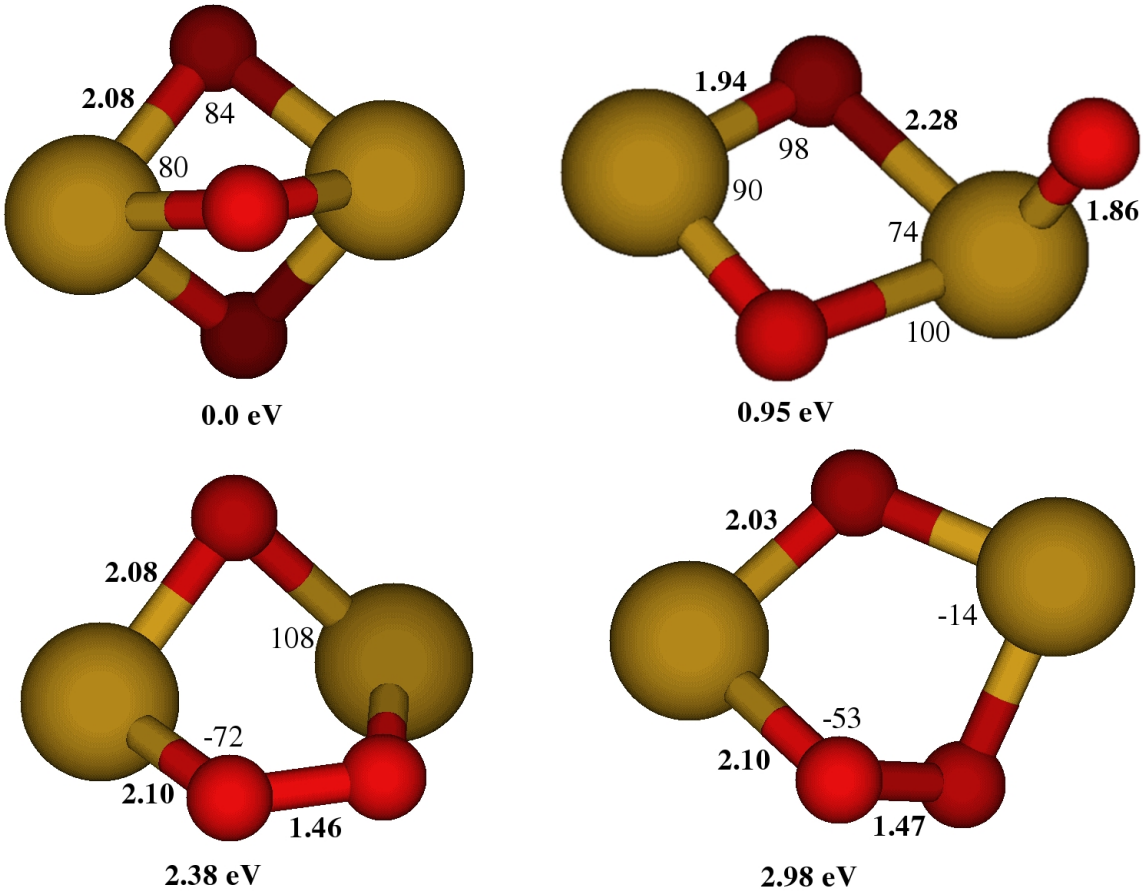

Figure 3.1.5: $^1Sb_2O_3$ neutral geometries. Underneath each is their energy relative to the ground state. Bond lengths are in angstroms (Å) and angles are in degrees. Dihedrals are denoted with a negative sign.

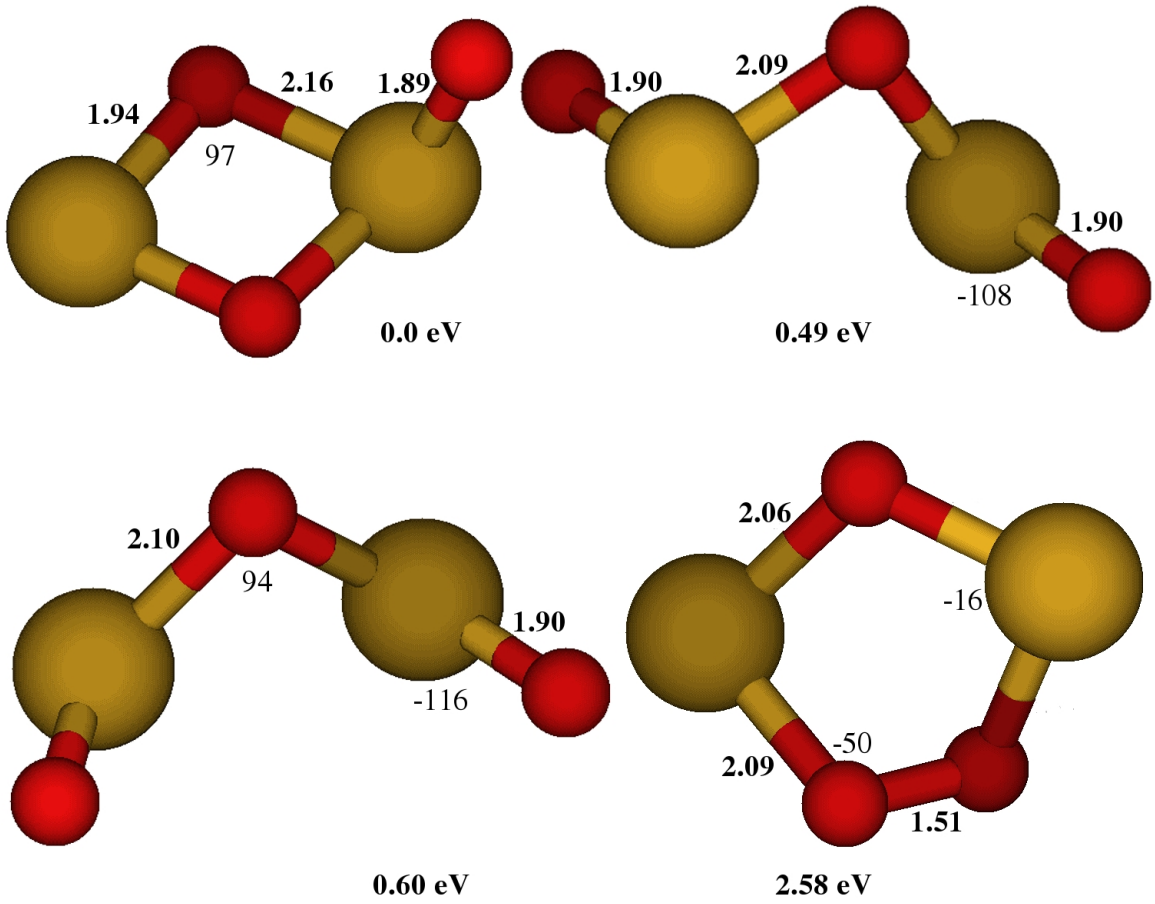

Figure 3.1.6: $^{2}Sb_2O_3^-$ anion geometries. Underneath each is their energy relative to the ground state. Bond lengths are in angstroms (Å) and angles are in degrees. Dihedrals are denoted with a negative sign.

What's interesting for the Sb_2O_3 clusters is that even at this microscopic size, the properties are already evolving towards those of the bulk. The crystalline structure of Sb_4O_6 exhibits a 93˚ O-Sb-O angle [37]. The same angle in the neutral Sb_2O_3 ground state geometry found here is 80˚ and in the first isomer are 74˚, 90˚, and 100˚. For the Sb-O bond lengths,

the bulk limit of 2.0 Å [37] was reached even at the SbO_2 level. Again with Sb_2O_3, there is only slight deviation from this bulk value. Another similarity reproduced in all low-lying states, neutral and anionic, is that the antimonies bind with oxygen only, not directly with other antimony atoms.

The energetics of the Sb_2O_3 clusters correlate well with experimental data extrapolated from photoelectron spectra (PES). The results are summarized in Table 3.1.5 and the spectra obtained by Ujjwal Gupta from Penn State is presented in Figure 3.1.7. The other theoretical study [37] is the same used for comparison with SbO: DZ-LCAO basis mixed with an ECP36 for Sb ECP2 for O, Vosko parametrization-LSDA functional. The ground state neutral geometry and binding energy ([37] didn't report anion optimization) agreed with the other theory. The VDE to ground state multiplicity was consistent with the PES. However, the AEA was not.

Sb_2O_3: Methods	**R^0**	**AEA**	**VDE(M-1)**	**VDE(M+1)**	**E^-_{atom}**	**E^0_{atom}**
GGA-DFT (This work)	2.08	1.42 (2.37)	2.59	3.65	3.51	4.21
Experiment (Penn State)	---	2.40	2.70	---	---	--
Other Theory[37]	2.03	---	---	---	---	4.33

Table 3.1.5: Sb-O bond length R (Å), adiabatic electron affinity AEA (eV) and in parentheses the difference in energy from the ground state anion to the first isomer neutral, vertical detachment energies VDE (eV) for transitions from the ground state anion with multiplicity M to the neutrals with multiplicities M-1 and M+1, and atomization energies E_{atom} (eV/atom) for the neutral and anionic Sb_2O_3.

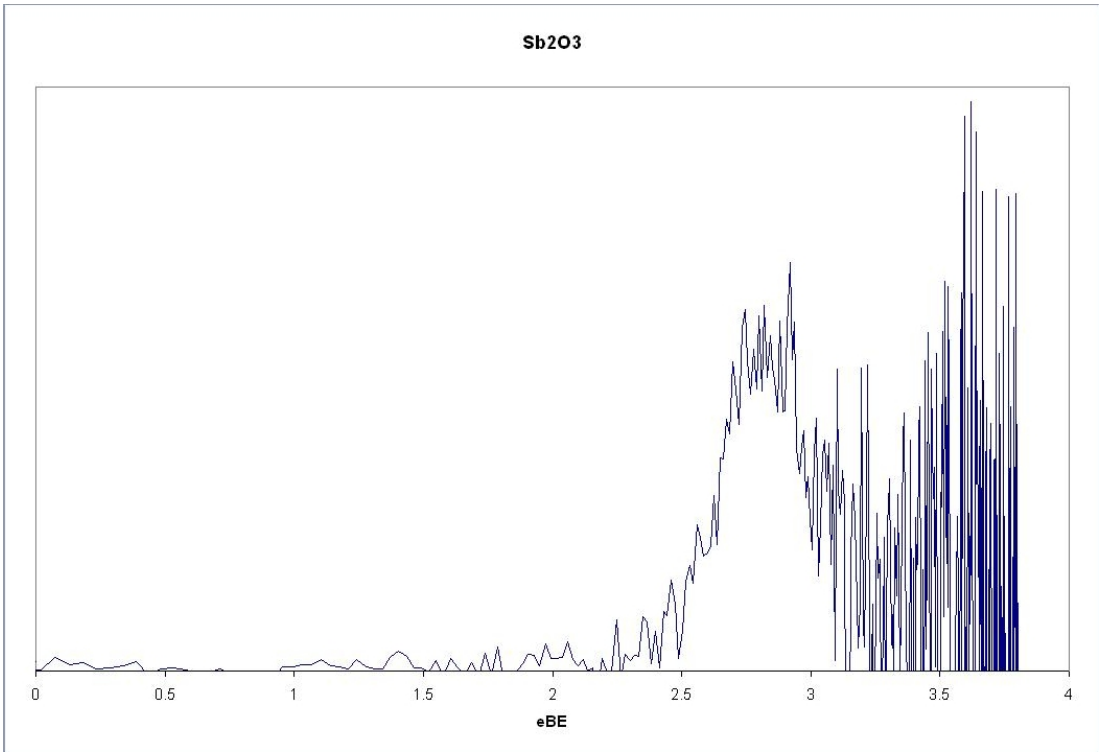

Figure 3.1.7: Photoelectron spectra for Sb_2O_3. The intensity (y-axis) is in arbitrary units and is plotted against the electron binding energy (eBE in eV).

The AEA discrepancy is likely the result of extended relaxation from the ground state anion to the neutral geometry. Looking at the PES spectra, the signal remains present, albeit at lower intensity, all the way to 1.0 eV. This indicates that the transition may be progressing through multiple configurations before stabilizing to the ground state or that multiple transitions are occurring. The peak around 1.4 eV is 5% of the maximum electron intensity and coincides nicely with the calculated AEA. The AEA threshold extracted from the maximum peak correlates with the transition energy calculated from

the ground state anion geometry to the neutral first isomer geometry (in parentheses in Table 3.1.5, AEA column).

Antimony oxides present the opportunity to understand the composition-dependence of properties which indicate electronic stability. Two parameters are major indicators of a cluster's electronic stability: the optical band gap and the atomization energy E_{atom}. Even though the Kohn-Sham orbitals do not represent true single-particle states, the difference between the highest occupied and lowest unoccupied molecular orbitals (HOMO-LUMO gap or HL-gap) provides a rough approximation the true optical band gap [m]. The stepwise evolution of the HL-gap and the E_{atom} for neutral Sb_2O_3 are presented in Figure 3.1.8. The HL-gap for the Sb_2O_3 cluster is already close to the direct gap of thin film Sb_2O_3, observed at room temperature to be 3.628 eV [29].

The comparisons made in this graph illuminate the importance of a closed shell electronic structure for the stability of clusters. We see that the replacement of an antimony with an oxygen (Sb_2 to SbO) increases the stability in terms of the atomization energy, but puts the HL-gap in free fall. The reason for the steep descent of the HL-gap is most likely due to the closed shell structure of neutral Sb_2 versus the open shell, doublet state of neutral SbO. Neutral SbO_2 is also a doublet, so while the addition of another oxygen further increases the energy required to break the cluster into its atom constituents, the HL-gap only increases by about 0.7 eV. Finally with Sb_2O_3, its superior stability is achieved with a closed shell structure, a high HOMO-LUMO gap, and a high atomization energy of 4.21 eV.

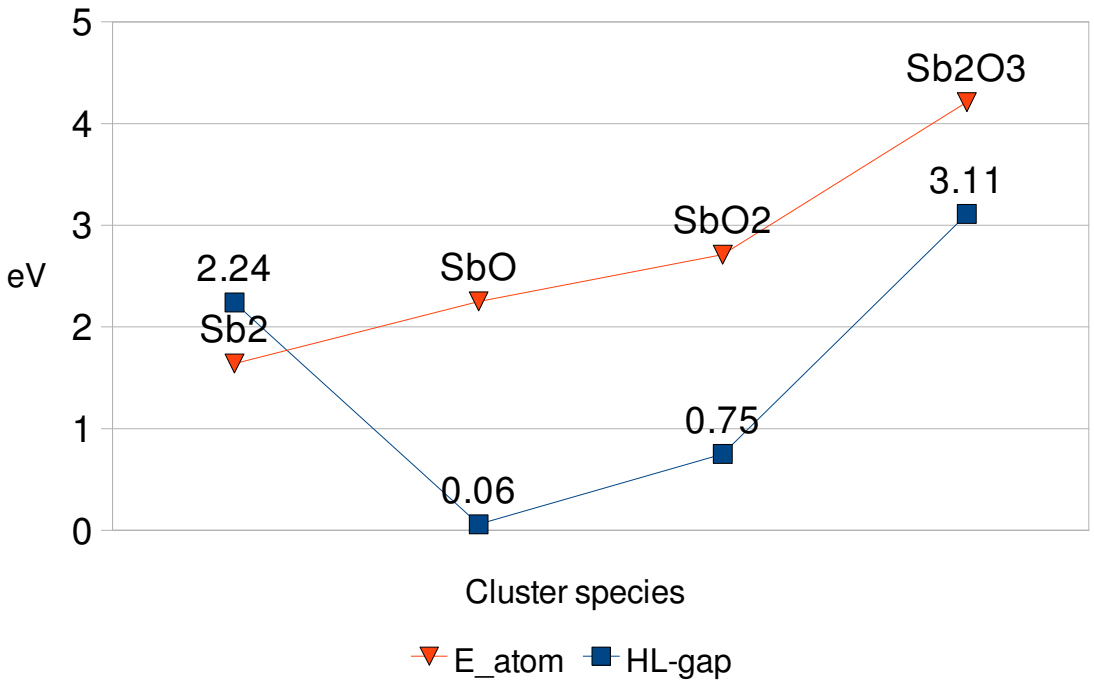

Figure 3.1.8: Composition-dependence of atomization energy E_{atom} (eV/atom) and the HOMO-LUMO gap (eV), an approximation of the direct optical band gap.

3.2 Bismuth and Lead Anions Solvated in Ammonia

Solvation is an extremely complicated process, but if we zoom into the molecular level we can uncover the interactions between the ion and the solvent molecule. Gas phase solvated ion clusters are model systems to explore intermolecular reactions. A limited number of solvent molecules actually interact with the metal solute [38]. Therefore, we can model an increasing number of solvent molecules around a core metal atom to see the stepwise size evolution of ion-neutral interactions as we move from the cluster level to solution. Detaching an electron from each system, in modeling and in experiment, enables study of the ensuing electronic transitions. Solvation studies aid understanding of phenomena such as nucleation and atmospheric stoichiometry.

Ammonia is the most widely-used and studied solvent other than water. Industrial processes require it for the synthesis of commercial and household cleaners, pharmaceuticals, and fertilizers. It is essential to the nutritional intake of plant life. In chemical studies, ammonia is used for inorganic analysis and to dissolve reactive metals such as zinc. The solvation of metal cations in ammonia, including K^+, Rb^+, Bi^+[39], Ag^+, Cu^+[40], Li^+, Na^+[41], and Pb^+[42], has been extensively studied by the Castleman group at Penn State. They have done so using mass spectrometry and thermodynamic measurements. Gleim *et al.* predicted a partial covalent interaction between Pb^+ and ammonia molecules due to finding a higher binding energy than would result from electrostatic interactions alone [42]. Indeed, ammonia presents a unique opportunity to determine properties resulting in different bonding mechanisms.

Ammonia is a polar molecule due to the relatively higher electronegativity of nitrogen. When bonded to form ammonia, the nitrogen is partially negative whereas the hydrogens are partially positive, illustrated in Figure 3.2.1. Due to this separation of charge, electrostatic forces are expected to chiefly contribute to intermolecular bonding with another polar or ionic molecule. On the other hand, the lone electron pair on nitrogen may become involved in covalent bonding with a neutral or open-shell atom or molecule.

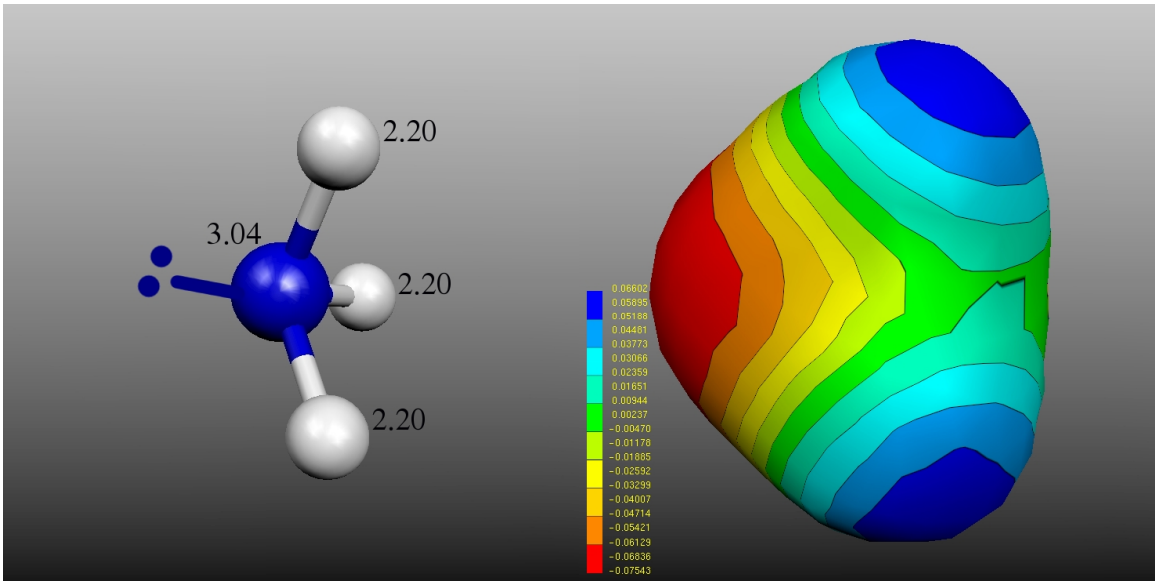

Figure 3.2.1: The difference in electronegativities (shown left with lone electron pair) of nitrogen and hydrogen causes a separation of charge on ammonia (right - red is -0.07 and blue is +0.06).

Ammonia's ground state is $^1A_1$ with C_{3v} trigonal pyramidal symmetry and a dipole moment of 1.847 Debye. Excited states have planar (trigonal bipyramidal including the lone electron pair) geometry assigned D_{3h} symmetry. This symmetry demarcation has to do with inversion, the process of nitrogen passing through the trigonal base to emerge on the other side thereby reversing the dipole. The potential barrier for inversion is only 6 kcal (2076 cm-1), so this process is suggested to occur frequently [43].

Lead and bismuth are the last two stable elements which are naturally occurring and non-radioactive, thus are frequently used in metal alloys and other commercial applications. Lead is frequently used in lead-acid batteries, as a dense material for bullets, radiation shielding, paint pigment, pewters, and solders. As the toxicity of lead becomes more worrisome, industries are substituting it with the nontoxic bismuth. Bismuth has many applications in its own right, including cosmetics, medicines such as Pepto-Bismol, and ceramics glazing. The ferroelectric material $BiFeO_3$ was recently found to enable the switching of current flow, making it attractive for a semiconductor diode in an electronic device [44]. The study also reported its ability to generate a photocurrent without external bias, which could be used to increase the efficiency of solar cell devices.

Because lead and bismuth are "heavy" atoms, spin-orbit coupling has a significant effect on their electronic structures. Lead and bismuth are main group metals of Group IV and Group V, respectively. Both have open 6*p*-shell configurations in the neutral state, lead having 2 valence electrons ($^3P_0$) and bismuth having 3 ($^4S_{3/2}$). Spin-orbit coupling is cited as the reason for the anomalous electron affinity of lead [45] and for the anomalous

ionization potential of bismuth [46]. Spin-orbit effects increase the spread of the relative energies for the ^3P_J states in neutral lead and the bismuth anion and cation. As a result, bismuth has a lower ionization potential (lower than lead) than predicted by effective nuclear charges. Lead's electron affinity is 1.05 eV lower when one splits the degeneracies of the ^3P energy level [45].

These spin-orbit corrections to the total energy are accounted for here using the spin-orbit (SO) collinear approximation under the Dirac formalism of the ADF code. To demonstrate the importance of including SO-corrections, DFT calculations were performed both with and without SO under a relativistic formulation. Comparison of these two routes are illustrated in Table 3.2.1. Notice in particular, in agreement with Ref. [v], Pb's electron affinity was lowered by about 1.05 eV by taking account of SO.

Photoelectron angular distributions (PADs) in velocity map images (VMI) depend upon the precursor orbital and the photoelectron's kinetic energy. The raw and reconstructed photoelectron velocity map images, produced by Mohamed Sohby at Penn State, are shown in Figure 3.2.2 and Figure 3.2.3 for Bi and Pb, respectively. The highest occupied molecular orbitals (HOMOs) of the anion species computed here are presented alongside the requisite VMI. For the atomic ions, detachment occurs from two orthogonal *p* orbitals. As illustrated in the computed HOMOs, these *p* orbitals seem to remain intact in the presence of one and two ammonias. If there is strong intermolecular interaction, the solvated species should exhibit PADs which are inconsistent with detachment from a *p* orbital.

For atomic Bi^-, the anisotropy parameter β of band X, the transition to the $^4S_{3/2}$ state, is close to the value of 0.42 observed by Polak *et al.* [47]. This value for β indicates a parallel distribution, consistent with detachment from a *p* orbital at high kinetic energy (in this case 1.4 eV). On the other hand, detachment from a *p* orbital at low kinetic energy should result in an isotropic distribution, which is exactly what we see for the transition marked A to the excited state $^2D_{3/2}$, whose β is close to zero [47].

The VMIs for Bi^- solvated in one and two NH_3 molecules show PADs that are consistent with detachment from an atomic *p* orbital. For the ground state transitions marked X, the PADs are perpendicular ($\beta \sim -1$), which is expected for detachment with intermediate kinetic energy. The excited state transitions are all isotropic, favorable for *p* orbital electrons detaching with low kinetic energy. This indicates that the solvent interaction with the bismuth core ion is very weak and the charge remains localized within the atomic orbital of the metal atom.

With the Pb^- series, solvation changes the character of the precursor orbital. The transitions of atomic Pb^- are consistent with detachment from a *p* orbital. The PAD for transition X to the $^3P_0$ ground state at high kinetic energy is parallel and the A and B transitions to $^3P_1$ and $^3P_2$ excited states at intermediate kinetic energy (~ 1 eV) show preferential perpendicular distribution. However with the solvated Pb^- species, the PADs are no longer consistent with *p* orbital detachment. The PADs of transitions X, A, and B in these cases are more isotropic.

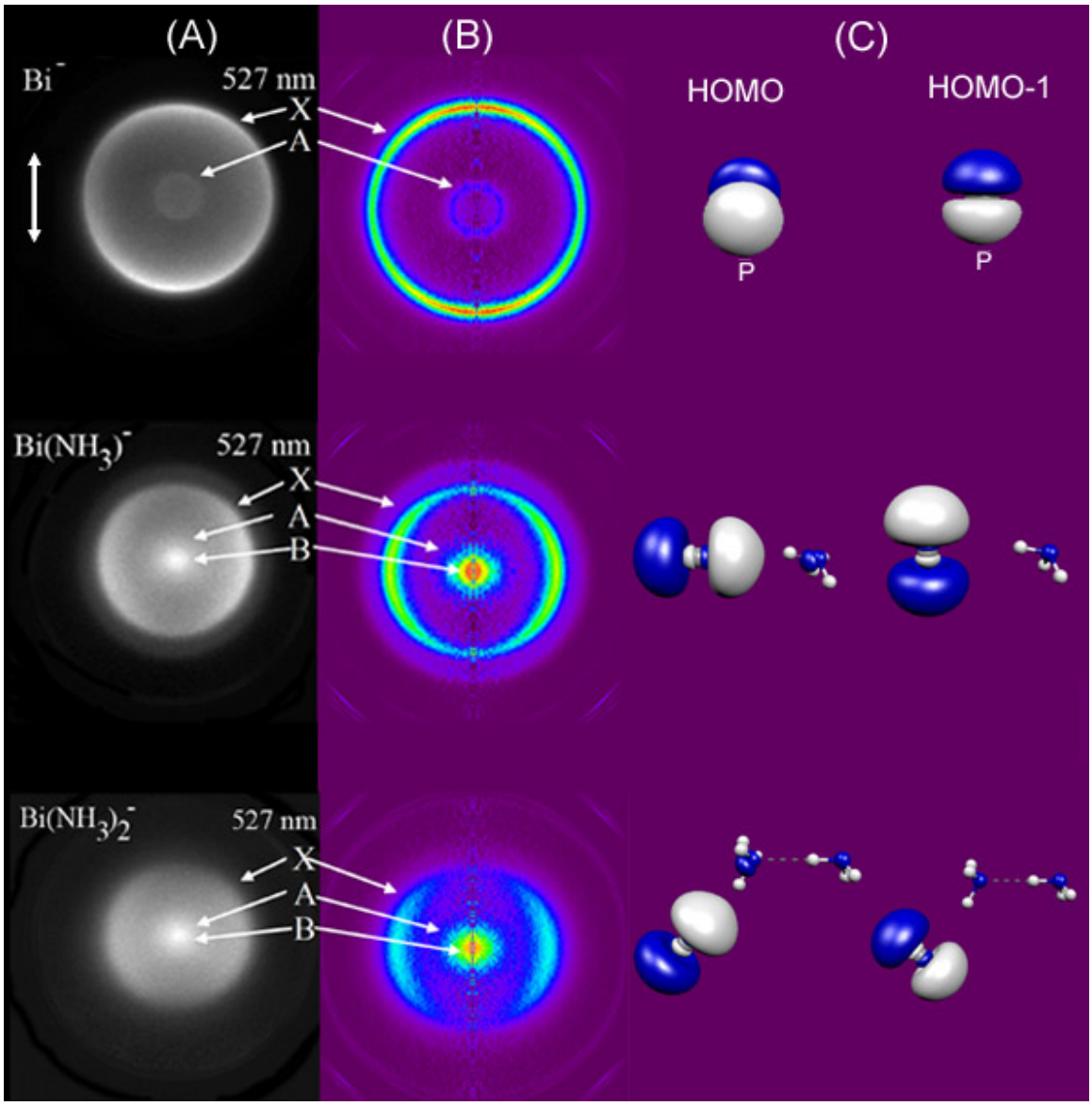

Figure 3.2.2: Raw (A) and reconstructed (B) photoelectron images of $Bi^-(NH_3)_n$ clusters (n = 0 - 2) obtained at 527 nm. The axis of light polarization is vertical in the image plane. Band X is the transition to the neutral ground state occurring at the lowest electron binding energy while A and B are transitions to excited states. The highest occupied molecular orbitals (HOMOs) are shown in (C).

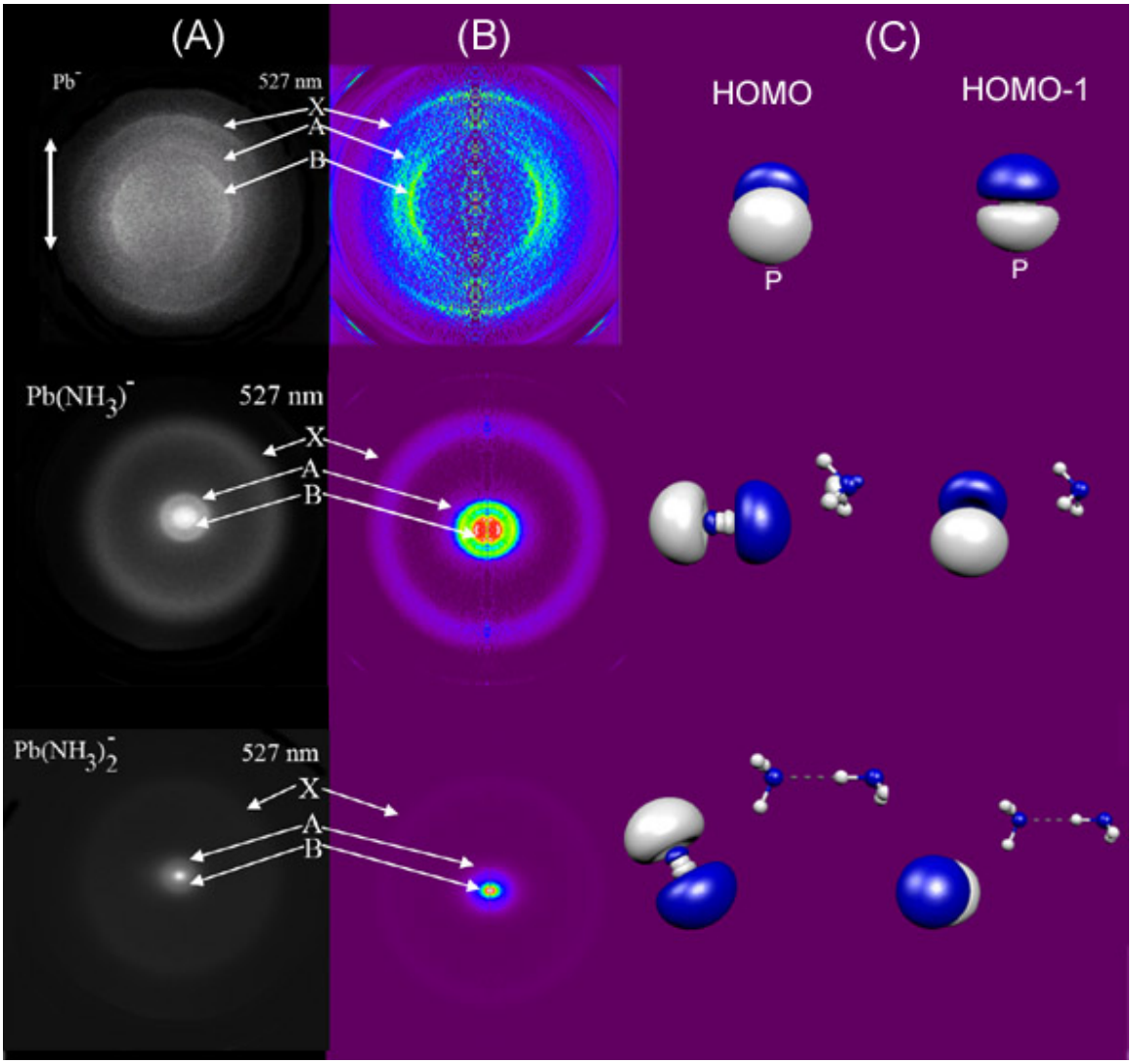

Figure 3.2.3: Raw (A) and reconstructed (B) photoelectron images of $Pb^-(NH_3)_n$ clusters (n= 0 - 2) obtained at 527 nm. The vertical double arrow indicates the axis of light polarization. The three transitions to accessible neutral states are marked X,A, and B. Band X is the transition to the neutral ground state occurring at the lowest electron binding energy while A and B are transitions to excited states. The highest occupied molecular orbitals (HOMOs) are shown in (C).

	AEA (Exp.)	VDE (Exp.)		AEA (Theo.) (SO)	VDE (Theo.) (SO)	AEA (Theo.) (SR)	VDE (Theo.) (SR)	
		X	*A*				M-1	M+1
$^3Bi^-$		0.947 ±0.01[a]	2.25	1.00	1.00	0.81	2.00	0.81
$^3Bi(NH_3)^-$	1.07	1.426	2.28	1.02	1.15	1.11	1.75	1.14
$^3Bi(NH_3)_2^-$	1.15	1.542	2.30	1.03	1.33	1.17	1.92	1.32
$^3Bi(NH_3)_3^-$				1.01	1.46	1.06	2.05	1.45
$Bi(NH_3)_4^-$				1.49	1.55	1.56	2.12	1.53
$^2Bi_2^-$				1.25	1.29	1.09	1.16	2.62
$^2Bi_2(NH_3)^-$				1.37	1.51	1.21	1.44	2.57
$^2Bi_2(NH_3)_2^-$				1.34	1.64	1.19	1.57	2.72
$^2Bi_2(NH_3)_3^-$				1.38	1.64	1.21	1.57	2.75
$^4Pb^-$		0.365 ±0.008[a]		0.27	0.27	1.33	1.33	8.02
$^4Pb(NH_3)^-$	0.60	0.98	2.26	0.70	0.78	0.82	1.49	6.61
$^4Pb(NH_3)_2^-$		1.00	2.31	0.68	0.93	0.73	1.64	6.10
$^4Pb(NH_3)_3^-$				0.65	0.98	0.67	1.72	5.34
$^4Pb(NH_3)_4^-$				0.75	1.06	0.79	1.81	4.93
$^2Pb_2^-$		1.366 ±0.01[b]		1.37	1.42	1.63	2.21	1.79
$^2Pb_2(NH_3)^-$				1.42	1.58	1.57	1.96	1.80
$^2Pb_2(NH_3)_2^-$				1.44	1.75	1.28	2.17	2.00
$^2Pb_2(NH_3)_3^-$	0.95	1.39	2.3	1.39	1.81	1.14	2.27	2.11

Table 3.2.1: Energetics of $M^-_m(NH_3)_n$ (M= Bi, Pb; m= 1-2; and n= 0-4) comparison between experimental and two types of theoretical results (Spin-orbit SO collinear approximation and Scalar Relativistic SR). Adiabatic electron affinities AEA and vertical detachment energies VDE are given in eV. a- Ref. [48] and b- Ref. [47].

For more on molecular-level interactions, we turn to cluster geometries optimized in the density functional formalism. As alluded to earlier with the discussion of ammonia's dipole moment, which atom in ammonia is closest to the metal atom indicates the dominant bonding mechanism. The geometries for low-lying states of neutral and anionic $Bi(NH_3)_n$ are presented in Figure 3.2.4. Notice in the anion species, the H ligands of ammonia point toward the Bi core. This indicates electrostatic forces dominate the bonding due to the positive end of the permanent dipole intersecting the H_3 base. When Bi is neutral, the N is the atom involved with the bonding. With the lone electron pair on N directly opposing the H ligands, this demonstrates a partial covalent interaction.

The same story unfolds with the optimized Pb geometries, depicted in Figure 3.2.5, the optimized Bi dimer geometries, Figure 3.2.6, and the optimized Pb dimer geometries, Figure 3.2.7. For both isomers and ground states, the same indications described for the Bi atom are present. This leads us to conclude that the bonding mechanisms are consistent throughout for the anion and neutral clusters, respectively.

As expected with solvation, the electron binding energy (AKA vertical detachment energy VDE in Table 3.2.1) increases with the number of solvent molecule. The PES spectra shown in Figure 3.2.8 for the Bi core with zero, one, and two ammonias aptly demonstrates this. Most important for the purposes of this study, the density functional calculations with spin-orbit corrections (SO) reproduced this trend (see Table 3.2.1). Further, this trend remains consistent with the dimer cases for which there were no experimental data to compare.

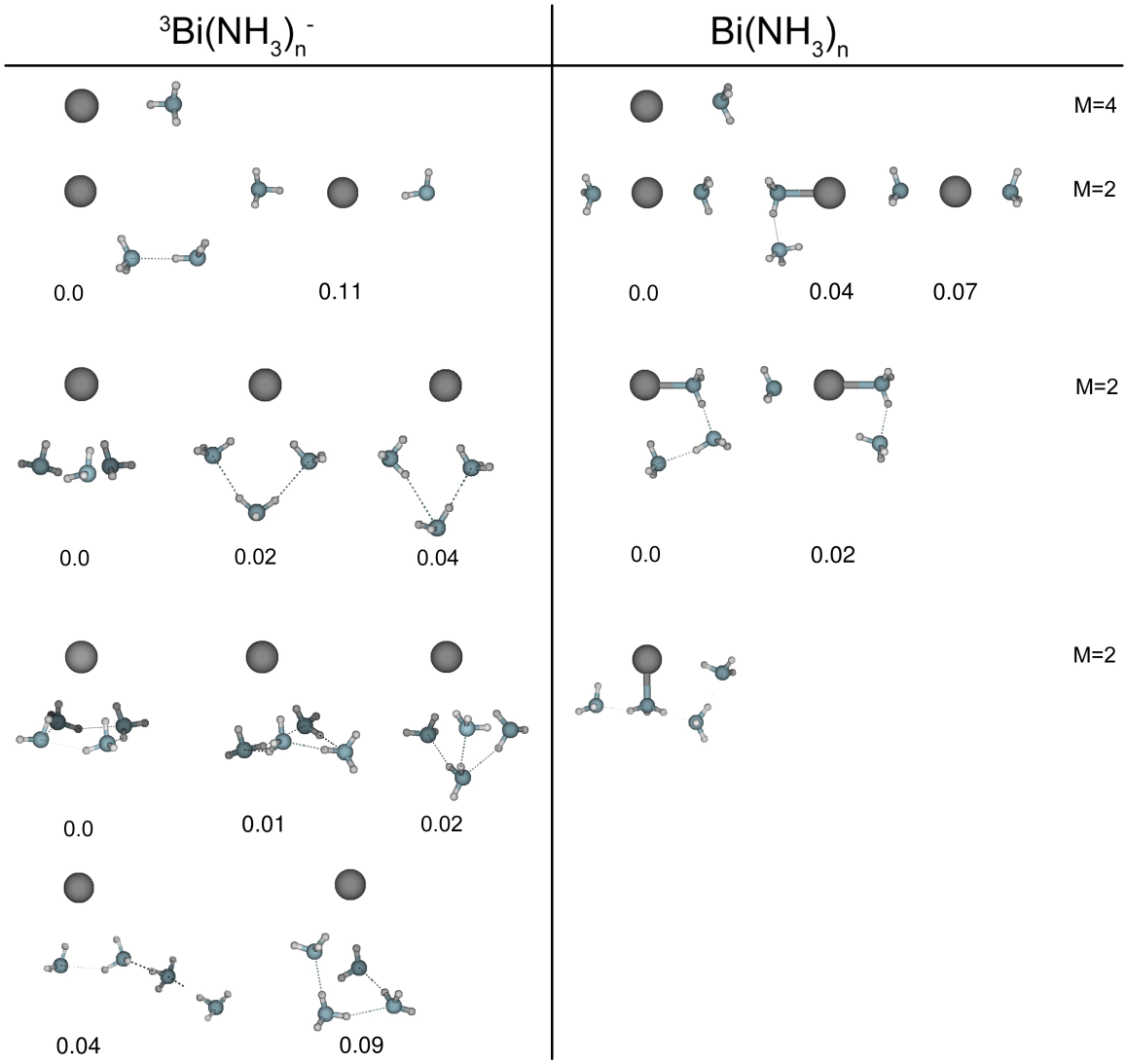

Figure 3.2.4: Geometries for low-lying states of $^3Bi^-(NH_3)_n$ (anions, left, spin multiplicity M = 3) and $Bi(NH_3)_n$ (neutrals, right, M varied with n). Relative energies to the ground state are below each cluster in eV unless no isomers were found.

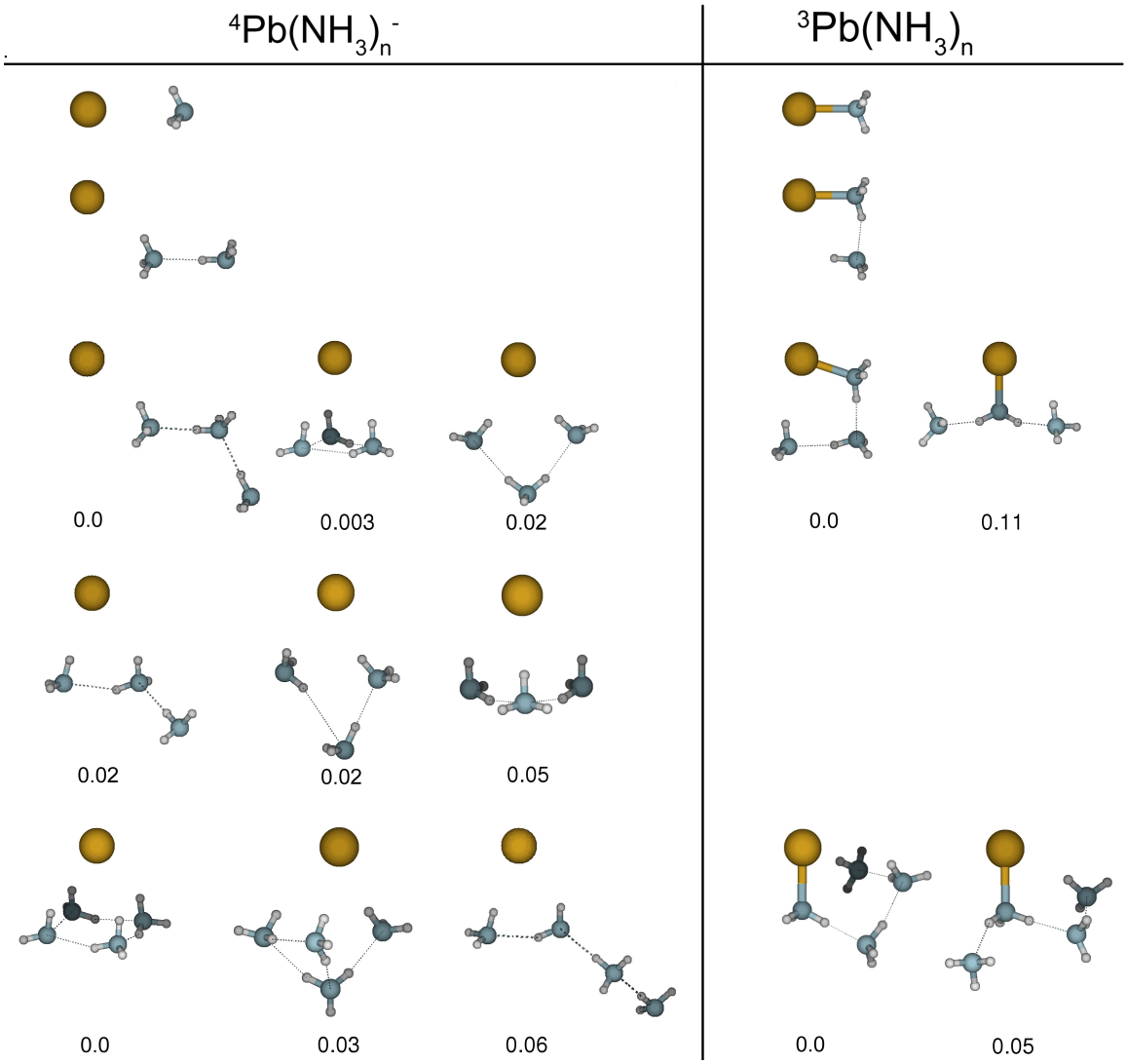

Figure 3.2.5: Geometries for low-lying states of $^4Pb^-(NH_3)_n$ (anions, left, spin multiplicity M = 4) and $^3Pb(NH_3)_n$ (neutrals, right, M = 3). Relative energies to the ground state are below each cluster in eV unless no isomers were found

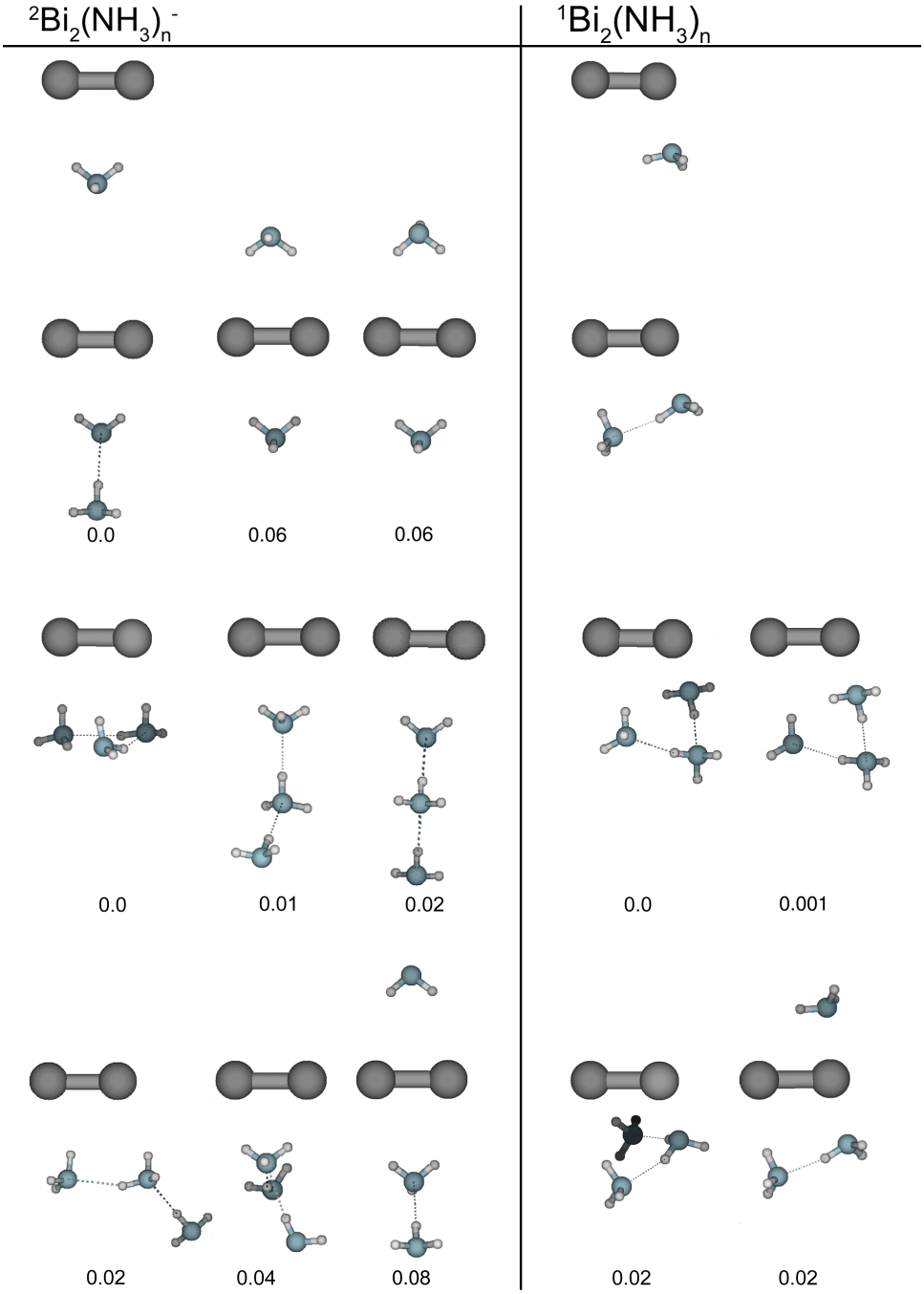

Figure 3.2.6: Geometries for low-lying states of $^2Bi^-(NH_3)_n$ (anions, left, spin multiplicity M = 2) and $^1Bi(NH_3)_n$ (neutrals, right, M=1). Relative energies to the ground state are below each cluster in eV unless no isomers were found.

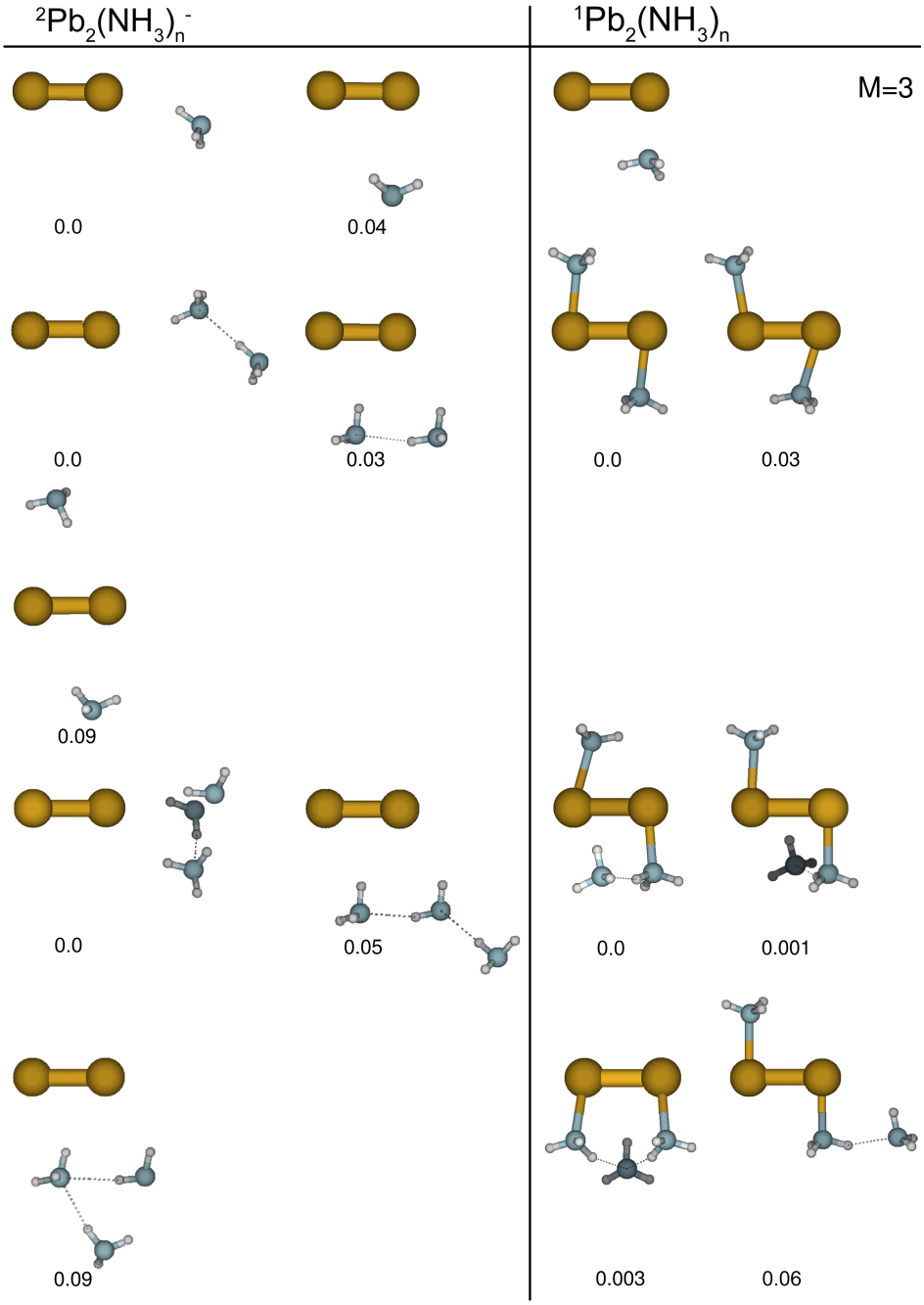

Figure 3.2.7: Geometries for low-lying states of $^2Pb^-(NH_3)_n$ (anions, left) and $^1Pb(NH_3)_n$ (neutrals, right, M = 3 for one NH_3 species). Relative energies to the ground state are below each cluster in eV unless no isomers were found.

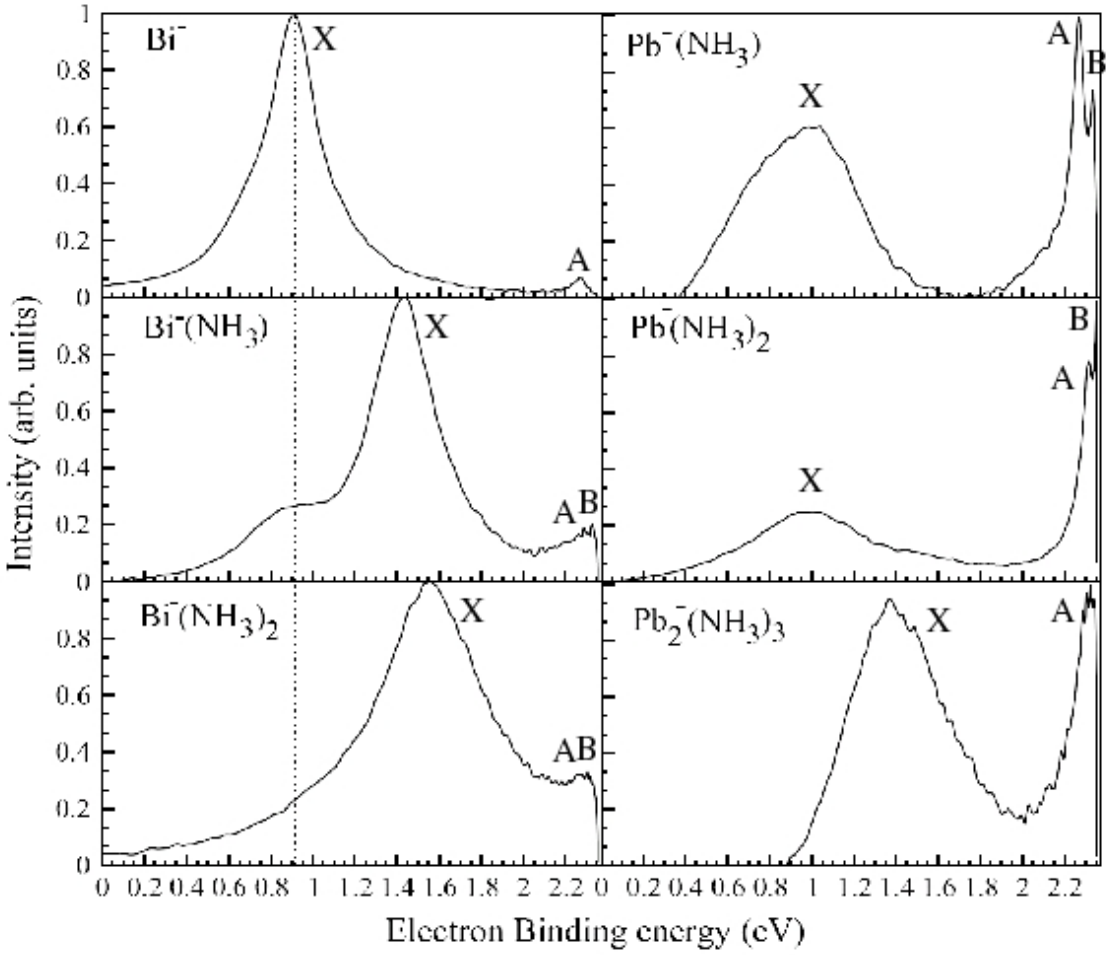

Figure 3.2.8: Photoelectron spectra of atomic Bi^-, $Bi^-(NH_3)_n$ and $Pb^-(NH_3)_n$ species at different levels of solvation (n= 1-2) as well as $Pb_2^-(NH_3)_3$. The spectra are normalized and plotted against the electron binding energy scale. The dotted vertical line coincides with the electron affinity of the Bi- atom. X marks the ground state transition and A and B are excited state transitions.

3.3 Silicon, Germanium, and Tin Quantum Dots

Quantum dots (QDs) are revolutionizing electronic technology; their quantum confinement makes optical and transport properties size and spacing dependent and thus tunable. They are naturally semiconducting devices with a wide array of applications such as light-emitting diodes [49], quantum computers [50], and contrast agents [1]. The tunable band structure and relatively low production cost of QDs makes them an attractive candidate for third generation solar cell technology. Tin (Sn) is a Group IV semiconductor [51] with such a potential but it has not previously been evaluated. Determining the electronic structure of Sn QDs is necessary for making accurate predictions about its behavior in the solar cell, designing the overall stack geometry and junction formation of the cell, as well as interpreting experimental data [52]. Here we explore the viability of Sn QDs as building blocks for solar cell materials using the density functional theory (DFT) in the Kohn-Sham (KS) and Hartree-Fock (HF) formalisms.

The elaborate shapes of the molecular orbitals (MOs) and nontrivial relativistic effects make clusters with atoms beyond the third row more difficult to handle with DFT. Theoretical calculations of heavy atoms are necessary to predict material candidates for technological applications and to develop a complete understanding of physical data. However, DFT results of heavy elements with accuracies reliable enough for technology development are noticeably absent in the literature. This need to find an optimum computational route for consideration of heavy atoms to a high degree of precision is

addressed directly. The accuracies and computational expenses of DFT methods have been investigated to determine the optimum route for the study of QDs containing fifth row chemical elements.

The benefits of finding the optimum DFT route to determine Sn's material properties are two-fold; the validated route will determine Sn's viability in the proposed solar device and will further be utilized to determine the properties of clusters containing other chemical elements beyond the third row. The approximants used for this investigation were H- and OH- terminated Si_{10}, $Ge_{10,}$ and Sn_{12} QDs. Si and Ge experiments being well-established in the literature, those served as references to ensure reasonable efficiency of the route before using it on to the more computationally expensive Sn QD. A reasonable efficiency is considered to be hours or possibly days. A route that requires months of computing would not be amenable to technology development.

Computational routes were tested for both geometric structure optimizations and the subsequent single-point energy calculations (opt//spE). Each route consists of a choice of HF or a hybrid functional and a basis set to describe the MOs (routes specified with the notation: functional/basis set). Less accurate functionals such as HF may accommodate the geometry optimization satisfactorily and much faster, but a more accurate route may still be needed for the spE calculation. In choosing these combinations, factors such as charge delocalization, polarization, and relativistic effects of the approximants need to be considered.

Hybrid functionals contain terms for the HF exact exchange energy with generalized gradient approximation (GGA) corrections to recover the correlation energy, or the difference between the true electronic energy and the HF-measured energy. Therefore, hybrids should be more accurate than HF or DFT alone in calculating electronic properties. However, we found the HF functional to be much more efficient and reasonably accurate for the geometry optimization route.

The hybrid functionals chosen for this study are B3LYP, B3PW91, and PBEPBE. As an example, the B3LYP exchange-correlation functional

$$E_{xc}^{B3LYP} = E_{xc}^{LSDA} + a_0(E_x^{HF} - E_x^{LSDA}) + a_x \Delta E_x^{B88} + a_c \Delta E_c^{LYP}$$

contains the correction to the LSDA's correlation of Lee, Yang, and Parr (LYP). In a commensurate fashion, Becke's 1988 exchange functional corrects the HF-LSDA exchange term. The coefficients in front of each term have been fitted to experiment by Becke, so in a sense the B3LYP and B3PW91 functionals are semi-empirical. The PBEPBE hybrid also has parameters, but those are derived from fourth-order perturbation theory to maintain the strictly numerical nature of DFT. These have been more elaborately discussed previously in §3.2 "Functionals in Practice."

The basis sets chosen here to expand the single-particle wavefunctions belong to two classes: all-electron and scalar-relativistic pseudopotential. Of the all-electron basis sets, the ones chosen for this study are the UGBS of de Castro, Jorge, *et al.*, three from the Pople group 3-21G*, 6-31G(d), and 6-311+G(2d,p), and DGDZVP by *DGauss*. The

UGBS is in principle universal; it contains relativistic corrections but is computationally intensive and unstable. The Pople group basis sets do not account for relativistic effects, but generally compute well. The pseudopotential basis sets chosen were Los Alamos effective core potentials (ECP's) LanL2MB (MB for minimal basis) and LanL2DZ (DZ for extended with two radial functions instead of the minimal one), and three basis sets from Stevens, Basch, and Krauss: CEP-4G, CEP-31G, and CEP-121G.

Key parameters such as bond lengths, the HL-gap which is the energy difference between the highest-occupied MO (HOMO) and the lowest-unoccupied MO (LUMO), the density of states, charge distribution, and ground-state absorption spectra have been calculated from the DFT results. The energetics were compared to high-level reference computations and experimental data for verification of the single point energy calculations. The accuracy of the geometry optimization was gauged by comparing the results of each route to high-level reference computations (B3LYP/6-311+G(2d,p)) and the experimental bond lengths. The most relevant results will be presented here.

Figure 3.3.1: Si-H and Si-OH bond lengths obtained from different DFT computational routes.

For $Si_{10}H_{16}$, the geometries with Si-H bond lengths closest to the experimental value 1.481 A [53] were optimized with the HF/DGDZVP, HF/3-21G*, HF/LanL2DZ, and B3LYP/LanL2DZ routes. The bond lengths of the different computational routes are presented in Figure 3.3.1. The LanL2MB and CEP-4G minimal basis sets were consistently far off from both the experimental value and the high-level calculation (1.492 A) no matter which functional was used, while their extended set counterparts LanL2DZ, CEP-31G, and CEP-121G were consistently much closer. This trend continues throughout the data, lending credibility to the increased accuracy of using extended basis sets. The functionals that delivered the most accurate geometric structure judging from the Si-H bond lengths were HF and B3LYP, with B3PW91 trailing only slightly behind but PBEPBE being very unreliable. The same HF routes that worked best for H-terminated Si also optimized the geometry of the $Si_{10}OH_{16}$ best when compared with the experimental Si-OH bond length 1.672 A [53] and the high-level calculation of 1.700 A. For OH-terminated Si however, B3LYP was only accurate with the all-electron sets.

Looking at the $Ge_{10}H_{16}$ data, again the HF functional paired with DGDZVP, LanL2DZ, and CEP-31G and CEP-121G were closest to the high-level reference value of the Ge-H bond length 1.542 A and the experimental value 1.5246 A [54]. The Ge-H bond lengths for the different computational routes are shown in Figure 3.3.2. The B3PW91/DGDZVP was also very close. For $Ge_{10}OH_{16}$, the closest fitting routes were HF with 3-21G*, DGDZVP or LanL2DZ and B3LYP/DGDZVP when compared with the high-level reference value 1.81 A and the experimental value 1.76 A for Ge-OH [55].

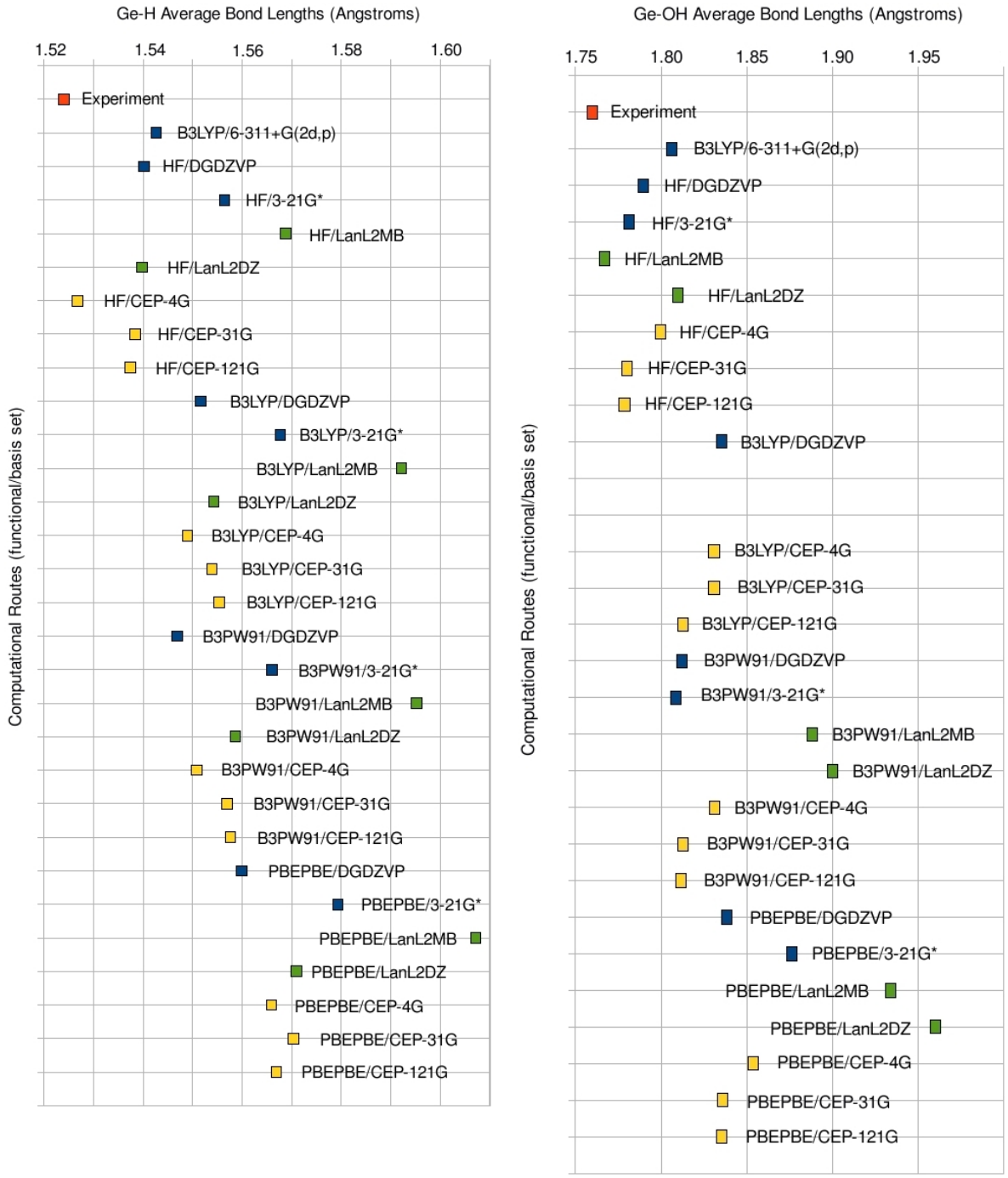

Figure 3.3.2: Ge-H and Ge-OH bond lengths obtained from different DFT computational routes.

For β-$Sn_{12}H_{24}$ geometries, the HF functional with LanL2DZ, CEP-31G and CEP-121G delivered the most accurate Sn-H bond length when compared with the experimental value 1.701 A [56]. We were not able to conduct the high-level all-electron reference route. None of the all-electron sets completed the geometry optimization within a reasonable amount of time or were unstable and would crash before finishing. Instead, we refer to the results we calculated for the Si and Ge approximants as well as experimental data where available. The Sn-H bond lengths for different computational routes are presented in Figure 3.3.3. The B3LYP functional with the same basis sets was also very close but the PBEPBE functional was unstable for the Sn approximant. The UGBS basis set, which has relativistic corrections and is theoretically supposed to work for all chemical elements, was unstable with all the approximants. From this it is concluded that the HF functional when paired with an extended pseudopotential basis set is the most feasible, in terms of accuracy and computation expense, for the geometry optimization route of heavy atoms.

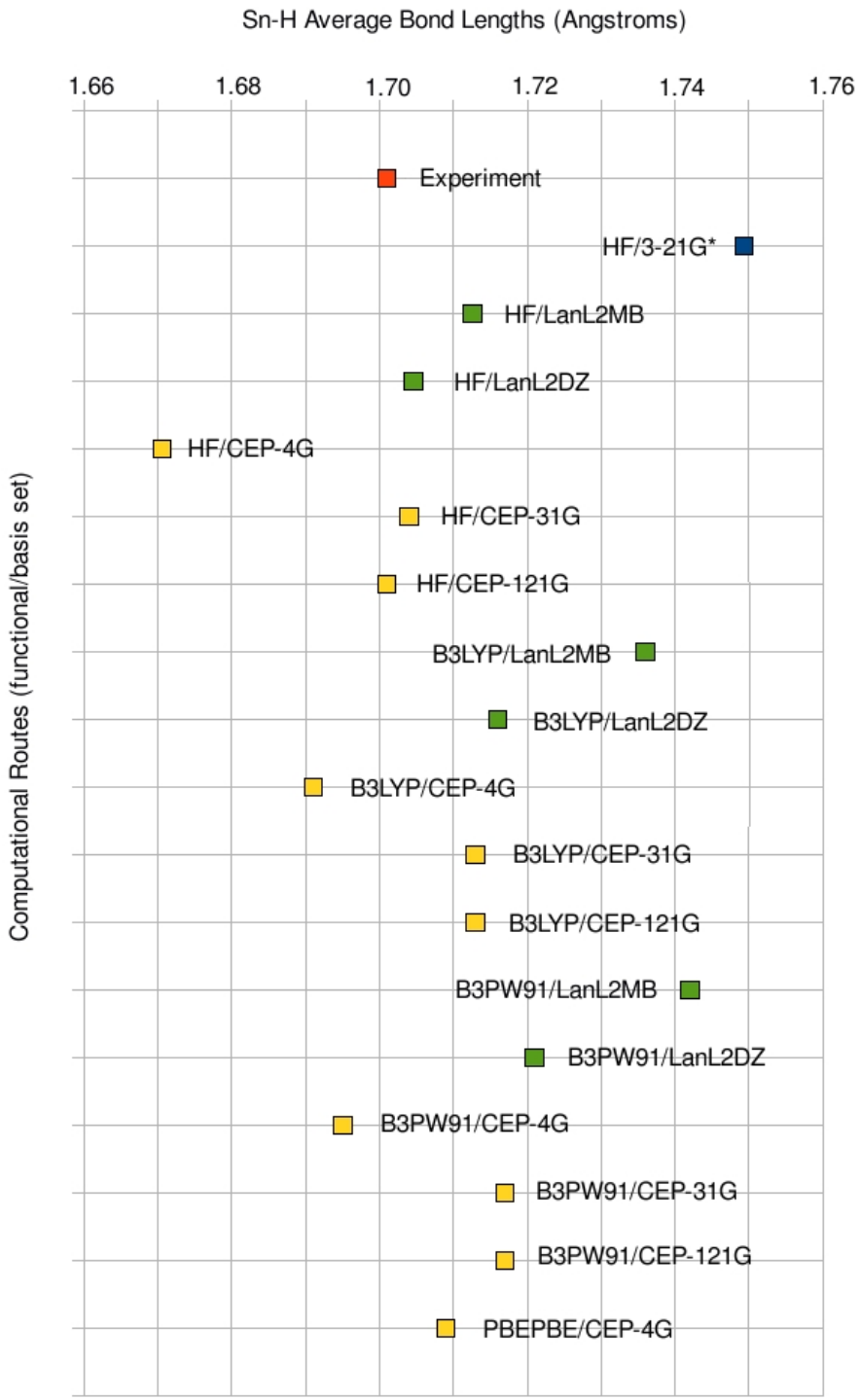

Figure 3.3.3: Sn-H bond lengths obtained from different computational routes.

For the spE calculations, the optimized geometries were used with different routes and the HL-gaps and density of states were compared with the high-level reference computational route B3LYP/6-31G(d)//B3LYP/6-311+G(2d,p). The density of states maps are shown in Figure 3.3.4 for $Si_{10}H_{16}$, in Figure 3.3.5 for $Ge_{10}H_{16}$, and in Figure 3.3.6 for $Sn_{12}H_{24}$. Excited state calculations are required for further experimental comparison and the time constraints of the program did not allow those to be undertaken. The most accurate route (opt//spE) in terms of these comparisons for the $Si_{10}H_{16}$ QD was found to be B3LYP/CEP-4G//B3LYP/CEP-121G. For the $Ge_{10}H_{16}$ QD, the optimum route contained the same spE route and the same functional for the opt route as for $Si_{10}H_{16}$, B3LYP/LanL2DZ//B3LYP/CEP-121G. For the Sn approximants, no reference value could be produced because the all-electron basis set would not be feasible.

From the results of the Si and Ge QDs, we concluded that the CEP basis sets are most likely the means of choice for Sn. As for the functional, the PBEPBE worked well for the Sn spE although it didn't for Si or Ge. This could be due to the fact that it works better for semi-local charge densities. The B3LYP functional was the most reliable in terms of both accuracy and efficiency for all the approximants. These optimum routes are being used to evaluate binary compounds with heavy atoms as material candidates for third generation hot carrier absorbers at the University of New South Wales, the host institution for this study. We were also able to determine through the literature that Sn may not be suitable for a material in a tandem solar cell device. While the band gap exists in these small cluster sizes, beyond 42 Sn atoms the band gap closes (see Figure 3.3.7).

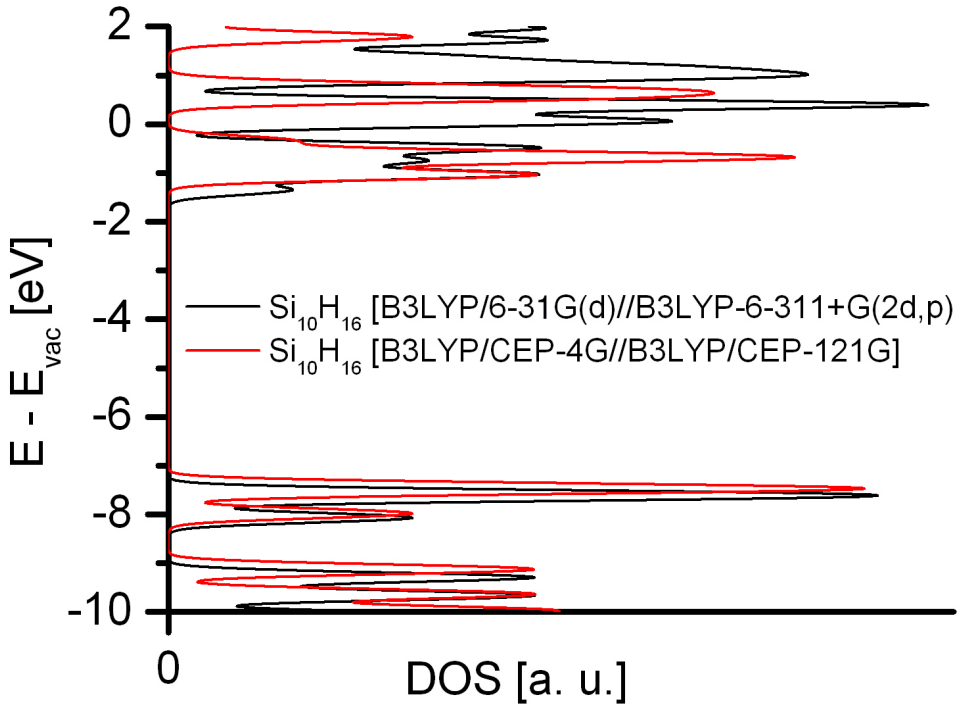

Figure 3.3.4: Density of states (DOS) for $Si_{10}H_{16}$ obtained from two DFT routes (opt// spE): the high-level reference containing 6-311+G(2d,p) and the more efficient closest match to the reference.

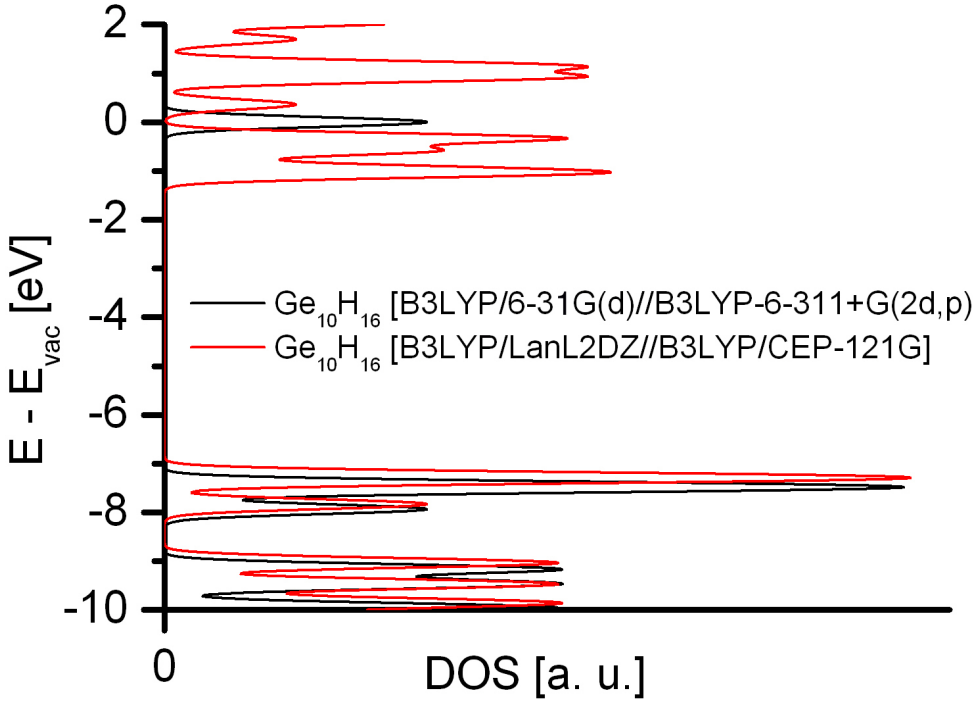

Figure 3.3.5: Density of states (DOS) for $Ge_{10}H_{16}$ obtained from two DFT routes (opt//spE): the high-level reference containing 6-311+G(2d,p) and the more efficient closest match to the reference.

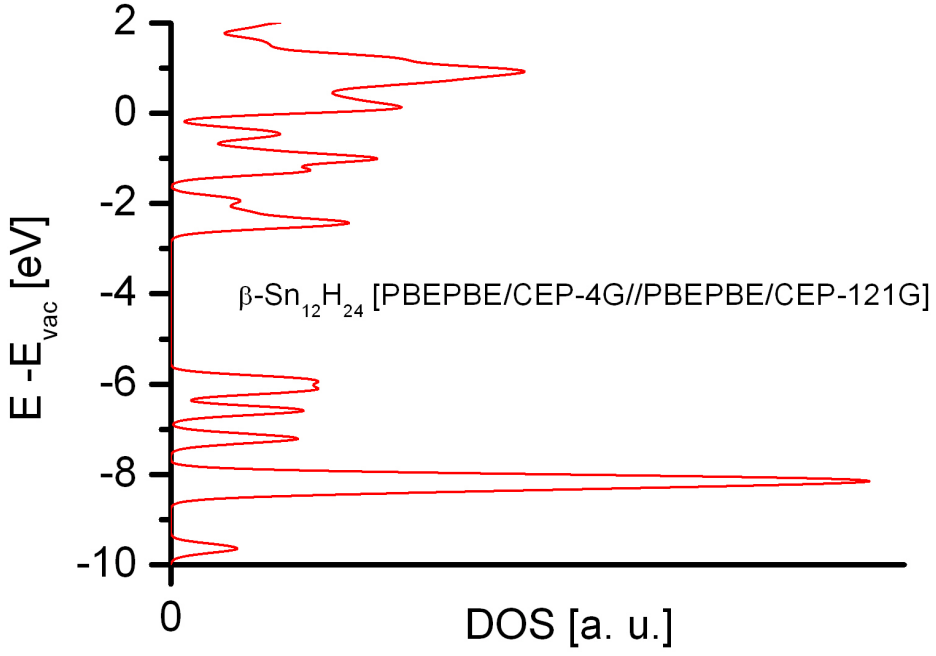

Figure 3.3.6: Density of states (DOS) for $Sn_{12}H_{24}$ obtained from the most likely optimum DFT route (opt//spE).

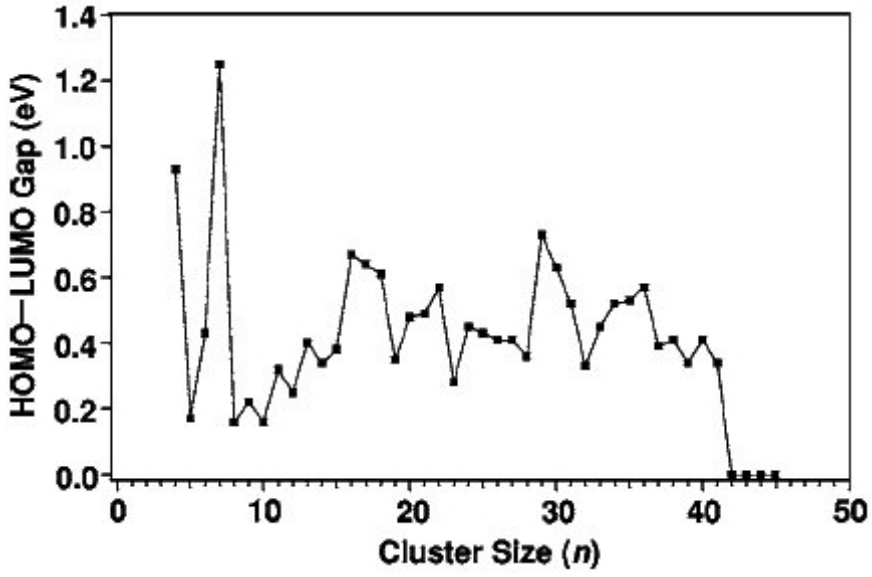

Figure 3.3.7: Experimental HL-gaps of Sn_n (n= 4-45) as function of cluster size [57].

Chapter 4. Conclusions

4.1 Summary

The promise to develop cluster assembled materials using cluster building blocks rests on our ability to identify stable motifs that will retain their identity upon assembly. In this thesis we have presented our findings on three classes of such systems, pure clusters, ligated clusters, and passivated clusters to explore their electronic properties, reactivities, and stabilities. Thus, we have been able to uncover their suitability for such assemblies as a function of cluster size and composition. Inevitably, we have shown that the properties of clusters are firmly dependent upon their electronic structure and that they change with cluster size, shape, and composition: different geometries of the same species yield different energies, closed-shell systems tend to be the most stable sizes.

Our studies on Sb_xO_y clusters (x=1,2; y = 0-3) show that the stability and the HOMO-LUMO gap can change dramatically with composition and size. Here Sb_2 has the lowest atomization energy per atom while SbO has the lowest HOMO-LUMO gap. On the other hand, Sb_2O_3 has a large atomization energy of 3.11 eV/atom and a large HOMO-LUMO gap of more than 4.0 eV. The HOMO-LUMO gap is larger than even in C_{60} (HOMO-LUMO gap of around 1.7 eV) that is known to form fullerides. Hence, we think that it may be a potential motif for such assemblies.

Cluster materials can also be formed by assembling ligated clusters in solution where the ligands can help prevent the collapse of the metallic clusters. Our work on Bi and Pb atoms and dimers coated with NH_3 shows that the ligands do not substantially alter the electronic states in metal motifs. Hence, such assemblies could be formed where the cores may be expected to retain its properties.

Finally I have explored the electronic structure of hydrogenated and hydroxylated Si_{10}, Ge_{10}, and Sn_{12} clusters to determine their viability as quantum dots for solar energy. I examined the Si and Ge quantum dots as a reference to uncover the most reliable DFT route, the combination of exchange-correlation functional and basis set which produced the most accurate results as compared to experiment while being computationally affordable. Our main finding is that the B3LYP functional and the CEP basis sets are the most reliable. Other basis sets not tested may be more accurate however. We also uncovered that Sn quantum dots would not be suitable for materials in tandem solar cell devices. Although small approximants have the desired band gap, at 42 atoms in size Sn goes from semiconducting to metallic.

References

[1] M.A. Green, *Physica E: Low-dim. Systems and Nanostructures,* **14,** 65 (2002).

[2] A.J. Nozik, *Annual Review of Physical Chemistry,* **52**, 193 (2001).

[3] X.H. Huang, I.H. El-Sayed, W. Qian, M.A. El-Sayed, *JACS*, **128**, 2115 (2006).

[4] M.C. Qian, S.V. Ong, S.N. Khanna, *et. al., Phys. Rev. B*, **75**, 104424 (2007).

[5] H.R. Hertz, *Annalen der Physik und Chemie,* **31**, 983 (1887).

[6] H.P. Bonzel, Ch. Kleint, *Progress in Surface Science,* **49**, 107 (1995).

[7] A. Einstein, *Annalen der Physik und Chemie*, **17**, 132 (1905).

[8] E. Surber, R. Mabbs, A. Sanov, *Journal of Physical Chemistry A,* **107,** 8215 (2003).

[9] J. Cooper, R.N. Zare, *Journal of Chemical Physics,* **48**, 942 (1968).

[10] M.A. Sohby, A.W. Castleman Jr., *Journal of Chemical Physics,* **126**, 154314 (2007).

[11] W.C. Wiley, I.H. McLaren, *Review of Scientific Instruments,* **26**, 1150 (1955).

[12] E. Surber, A. Sanov, *Journal of Chemical Physics,* **116**, 5921 (2002).

[13] A.W. Castleman Jr., R.G. Keesee, *Science,* **241**, 36 (1988).

[14] M.A. Sohby, K.A. Casalenuovo, J.U. Reveles, U. Gupta, S.N. Khanna, A.W. Castleman Jr., "Photoelectron imaging and density-functional investigation of Bismuth and Lead anions solvated in ammonia clusters." *(to be published)*

[15] J. Melko, Castleman Group, Penn State (private correspondence).

[16] K. Capelle, *Brazilian Journal of Physics,* **36,** 1318, (2006).

[17] C. Trindle, D. Shillady, *"Electronic Structure Modeling: Connections Between Theory and Software"* (CRC Press, Boca Raton, FL) 2008.

[18] C. Eckart, *Physical Review,* **36,** 878 (1930).

[19] P. Hohenberg, W. Kohn, *Physical Review B,* **136,** 864 (1964).

[20] R.M. Martin, "*Electronic Structure: Basic Theory and Practical Methods*" (Cambridge University Press, Cambridge, UK) 2004.

[21] J.P. Perdew, K. Burke, M. Ernzerhof, *Physical Review Letters,* **77,** 3865 (1996).

[22] A.D. Becke, *Journal of Chemical Physics,* **98**, 5648 (1993).

[23] J.P. Perdew, M. Ernzerhof, K. Burke, *J. Chem. Phys.,* **105**, 9982 (1996).

[24] *Gaussian 03*, Revision D.01, M. J. Frisch, G. W. Trucks, H. B. Schlegel, G. E. Scuseria, M. A. Robb, et al., Gaussian, Inc., Wallingford CT (2004).

[25] *deMon2k*, A.M. Köster, P. Calaminici, M.E. Casida, R. Flores-Moreno, G. Geudtner, A. Goursot, T. Heine, A. Ipatov, F. Janetzko, J.M. del Campo, S. Patchkovskii, J.U. Reveles, D.R. Salahub, A. Vela, deMon developers (2006).

[26] *ADF 2008.01*, E.J. Baerends, J. Autschbach, A. Bérces, F.M. Bickelhaupt, C. Bo, SCM, Theoretical Chemistry, Vrije Universiteit, Amsterdam, The Netherlands, http://www.scm.com (2008).

[27] H. Zhang, K. Sun, Z. Feng, P. Ying, C. Li, *Applied Catalysis A,* **305,** 110 (2006).

[28] D.H.E. Kunz, *Makromolekulare Chemie-Macromolecular Symposia,* **74,** 155 (1993).

[29] N. Tigau, V. Ciupina, G. Prodan, *Journal of Crystal Growth,* **277**, 529 (2005).

[30] H. Bryngelsson, J. Eskhult, L. Nyholm, M. Herranen, O. Alm, K. Edstrom, *Chemistry of Materials,* **19,** 1170 (2007).

[31] J.C. Jumas, M. Womes, P.E. Lippens, J. Olivier-Fourcade, *Hyperfine Interactions,* **182,** 103 (2008).

[32] K. Liu, J. Zhai, L. Jiang, *Nanotechnology,* **19,** 165604 (2008).

[33] E.P.F. Lee, J.M. Dyke, F.T. Chau, *et. al., J. Chem. Physics,* **125,** 064307 (2006).

[34] X. Zhou, J. Zhao, X. Chen, W. Lu, *Physical Review A,* **72**, 053203 (2005).

[35] M. Gausa, R. Kaschner, G. Seifert, *et. al., J. Chem. Phys.*, **104**, 9719 (1996).

[36] M.L.Polak, G. Gerber, J. Ho, W.C. Lineberger, *J. Chem. Phys.*, **97**, 8990 (1992).

[37] B.V. Reddy, P. Jena, *Chemical Physics Letters,* **288,** 253 (1998).

[38] A.W. Castleman, Jr., S. Wei, *Annu. Rev. Phys. Chem.*, **45**, 685 (1994).

[39] A.W. Castleman, Jr., *Chem. Phys. Lett.* **53**, 560 (1978).

[40] P.M. Holland, A.W. Castleman, Jr., *J. Chem. Phys.* **76,** 4195 (1982).

[41] A.W. Castleman, Jr., P.M. Holland, D.M. Lindsay, K. Peterson, *J. Am. Chem. Soc.* **100**, 6039 (1978).

[42] K.L. Gleim, B.C. Guo, R.G. Keesee, A.W. Castleman, Jr., *Journal of Physical Chemistry,* **93**, 6805 (1989).

[43] S.H. Bauer, Structural Chemistry, **18**, 959 (2007). Accessed online at http://www.springerlink.com/content/v7617k40335n3271/

[44] T. Choi, S. Lee, Y.J. Choi, V. Kiryukhin, S.-W. Cheong, *Science*, **324**, 63 (2009).

[45] J.A. Chamizo, *Journal of Chemical Education*, **61**, 874 (1984).

[46] D.W. Smith, *Journal of Chemical Education*, **52**, 576 (1975).

[47] M.L. Polak, J. Ho, G. Gerber, W.C. Lineberger, *J. Chem. Phys.* **95**, 3053 (1991).

[48] C.S. Feigerle, R.R. Corderman, W.C. Lineberger, *J. Chem. Phys.* **74**, 1513 (1981).

[49] A. Karim, G.V. Hansson, W.-X. Ni, P.O. Holtz, M. Larsson, H.A. Atwater, *Optical Materials,* **27,** 836 (2005).

[50] J. Kouvetakis, J. Menendez, A.V.G. Chizmeshya, *Annual Review of Materials Research,* **36,** 497 (2006).

[51] C.W. Jiang, M.A. Green, *Journal of Applied Physics,* **99,** 114902 (2006).

[52] *ARC Photovoltaics Centre of Excellence*, Annual Report (2006). Accessed online at <http://www.pv.unsw.edu.au/research/annualreports.asp>

[53] Z. Jing, J.L. Whitten, G. Lucovsky, *Physical Review B*, **45,** 13978 (1992).

[54] K. Ohno, M. Kawamura, H. Matsuura, *J. Sci. Hiroshima Univ. A, Phys. Chem.,* **49,** 1 (1985).

[55] A. Koebbel, M. Polcik, D.R. Lloyd, *et al.*, *Surface Science*, **540,** 246 (2003).

[56] G.R. Wilkinson, M.K. Wilson, *Journal of Chemical Physics*, 784 (1956).

[57] L.F. Cui, L.M. Wang, L.S. Wang, *J. Chem. Phys.*, **126,** 064505 (2007).

Vitae

Kristen Angelina Casalenuovo was born August 31, 1984 in Lynchburg, Virginia. After graduating from Rustburg High School in 2002, she attended Longwood University in Farmville, Virginia where she earned a Bachelor of Science in Physics, summa cum laude, under the advisement of Dr. Charles Ross. During her undergraduate years, she investigated cosmic ray activity with several other Longwood students and Dr. Ross. She also participated in a National Science Foundation (NSF) summer Research Education for Undergraduates program at the University of Maryland. There she conducted research on chaotic scattering for Dr. James Yorke, giving a university-wide presentation at the conclusion titled "Air Hockey Implies Chaos." Kristen had the great fortune of expanding her cultural horizons, studying abroad her junior year in Florence, Italy.

While pursuing her Master of Science, Kristen's research efforts at Virginia Commonwealth University provided her the opportunity to present at the American Physical Society March Meeting in 2009 on "Photoelectron Imaging and Density Functional Investigation of Bismuth and Lead Anions Solvated in Ammonia Clusters." Her crowning achievement was being selected for the NSF East Asia and Pacific Summer Institute program in Australia. There she applied her knowledge of density functional theory to the characterization of materials for third generation solar cell technology at the School of Photovoltaic and Renewable Energy Engineering with Dr. Dirk König. Kristen looks forward to continuing her education and research at the PhD level.